energies

MDPI

Article

Determining the Valid Petrophysical Threshold of Interbedded Sandstone Reservoirs in Shale: The Role of Source–Reservoir Assemblage and Divergence from Conventional Reservoirs

Shujun Yin [1,2,3], Jiandong Zheng [1,2,3,*], Limin Fang [4], Jin Hu [5], Zhongrui Wang [6,*], Zhaoqian Zhang [1,2,3], Wenjuan Wang [1,2,3], Guiwen Wang [6] and Peng Xie [1,2,3]

1 State Key Laboratory of Continental Shale Oil, Daqing 163712, China; yinshujun@petrochina.com.cn (S.Y.); zhangzhaoqian1@petrochina.com.cn (Z.Z.); 1985wangwenjuan@petrochina.com.cn (W.W.); xiepeng2@petrochina.com.cn (P.X.)
2 Heilongjiang Provincial Key Laboratory of Continental Shale Oil, Daqing 163712, China
3 Exploration and Development Research Institute, PetroChina Daqing Oilfield Co., Ltd., Daqing 163712, China
4 Exploration Department of PetroChina Daqing Oilfield Co., Ltd., Daqing 163453, China; fanglimin@petrochina.com.cn
5 PetroChina Daqing Oilfield Co., Ltd., Daqing 163458, China; dlts_hujin@petrochina.com.cn
6 College of Geosciences, China University of Petroleum (Beijing), Beijing 102249, China; wanggw@cup.edu.cn
* Correspondence: zhengjd@petrochina.com.cn (J.Z.); rui282611@163.com (Z.W.)

Abstract

Shale oil stands as a critical growth engine for global unconventional hydrocarbon exploration and production. Sandstone interlayers within shale successions have become the primary reservoir units and key development intervals for interbedded shale oil plays due to their superior storage and seepage capacity relative to the shale matrix. Nevertheless, conventional petrophysical cutoff standards for effective reservoirs are mostly derived from independent conventional sandstone reservoirs, largely ignoring the controlling effect of source–reservoir configuration on hydrocarbon charging. This has resulted in a widespread paradox in production practices and severely constrained accurate resource assessment and efficient sweet spot delineation. To cover this gap, this study integrates thin section analysis, organic geochemical experiments, core petrophysical measurements, and geophysical logging data to systematically characterize the geochemical features of source rocks and the petrophysical properties of sandstone reservoirs. Then, a quantitative source–reservoir coupling index is established by integrating key controlling factors, including total organic carbon content, free hydrocarbon content, vitrinite reflectance, source–reservoir pressure difference, source–reservoir distance, and configuration relationship. According to the index, source–reservoir coupling relationships are categorized into strong, moderate, and weak grades. The corresponding petrophysical lower limits for effective sandstone reservoirs are determined hierarchically. The results indicate that threshold values increase with decreasing coupling intensity: strongly coupled systems have lower limits of 6.5% porosity and 0.12 mD permeability, while moderately coupled systems require higher thresholds of 8.5% porosity and 0.23 mD permeability. This study breaks through the limitations of traditional empirical methods that define reservoir cutoffs solely by porosity and permeability. A method and corresponding criteria for evaluating the petrophysical cutoffs of sandstone reservoirs were established for the study area. This enables effective identification of relatively low-quality sandstone reservoirs that can still form commercial oil accumulations under robust hydrocarbon supply conditions.

Academic Editor: Krzysztof Skrzypkowski

Received: 1 September 2026
Revised: 29 September 2026
Accepted: 9 October 2026
Published: 3 November 2026

Copyright: © 2026 by the authors. Licensee MDPI, Basel, Switzerland. This article is an open access article distributed under the terms and conditions of the Creative Commons Attribution (CC BY) license.

This also significantly improves the accuracy of effective reservoir recognition and sweet spot prediction in interbedded shale oil systems.

Keywords: petrophysical threshold; interlayered sandstones; source–reservoir assemblage; shale

1. Introduction

With the massive consumption of conventional oil and gas resources around the world, unconventional oil and gas has become an important successor direction in the energy field [1–3]. The successful practice of the "shale revolution" in North America has led to a global boom in shale oil exploration and development. Unconventional oil and gas resources are reshaping the global energy supply pattern [4], providing a valuable reference value for the exploration and development of global unconventional oil and gas resources [5–7]. Shale oil has abundant reserves around the world, and more than 100 areas contain shale [8]. The Midland and Delaware basins of the Permian Basin constitute the world's largest shale-oil-producing region, with production derived primarily from the Wolfcamp, Bone Spring, and Spraberry successions [9,10]. The Williston Basin hosts a representative marine shale oil system characterized by shale interbedded with dolostone and siltstone, most notably within the Bakken petroleum system [11,12]. The Eagle Ford play in the Gulf Coast Basin represents another archetypal marine shale oil system [13,14]. Other major shale-oil-producing regions outside China include the Denver–Julesburg and Anadarko basins in the United States, the Western Canada Sedimentary Basin in Canada, the Neuquén Basin in Argentina, and the West Siberian Basin in Russia [15–20]. In recent years, substantial advances have also been made in shale oil and shale gas exploration in China, particularly in the Ordos, Junggar, Bohai Bay, and Songliao basins [21–24]. The Songliao Basin hosts a national demonstration project for continental shale oil development. Organic-rich shales of the Cretaceous Qingshankou Formation are extensively developed throughout the basin and constitute a major shale-oil-producing succession in the Daqing Oilfield [25–28].

A range of methods has been developed to determine petrophysical cutoffs for sandstone reservoirs, principally including empirical–statistical, laboratory experimental, and production-performance-based approaches [29–31]. Empirical–statistical approaches commonly derive effective reservoir cutoffs from core porosity–permeability relationships, oil-bearing grades, and well-test results using probability distributions, cross-plots, or empirical regression. These approaches are straightforward and readily applicable in data-rich, relatively homogeneous reservoirs; however, the resulting cutoffs are commonly field- or basin-specific and can be sensitive to sample size and subjective interpretation [32]. Laboratory experimental approaches employ high-pressure mercury intrusion, rate-controlled mercury intrusion, nuclear magnetic resonance, oil–water relative permeability measurements, and displacement experiments. Cutoffs are then constrained using parameters such as displacement pressure, effective pore-throat radius, movable fluid saturation, and flow capacity. These approaches provide mechanistic insights into reservoir effectiveness from the perspectives of pore-throat architecture and fluid mobility but are limited by high experimental costs, the restricted representativeness of core-scale measurements, and the difficulty of reproducing in situ reservoir conditions [33–35]. Production-performance-based approaches define the cutoff as the minimum petrophysical condition required to obtain commercial oil flow or economically viable production, based on formation-testing, pilot production, or long-term production data. Although these approaches provide the most direct link to actual reservoir performance, the derived cutoffs

can be strongly influenced by stimulation intensity, completion design, production pressure drawdown, and economic constraints. Shale oil reservoirs, however, are characterized by pronounced multiscale heterogeneity and low porosity and permeability. Their oil enrichment and productivity are controlled not only by sandstone petrophysical properties but also by hydrocarbon supply from adjacent source rocks and source–reservoir spatial configuration. Consequently, conventional approaches based primarily on individual reservoir parameters or production responses have limited applicability to these systems [36,37]. These limitations motivate further evaluation of cutoff schemes that jointly consider source–reservoir assemblage, hydrocarbon generation and expulsion capacity, and sandstone storage and flow properties [38].

Current reservoir evaluation commonly relies on conventional "uniform porosity–permeability cutoffs" without adequately considering the spatial configuration between source and reservoir rocks [32]. Source–reservoir configuration exerts a primary control on shale oil enrichment, and the intimate coexistence of source and reservoir rocks is a defining characteristic of shale oil systems [39]. The source-to-reservoir distance and the type of source–reservoir configuration can alter the minimum conditions required for effective hydrocarbon storage, thereby constraining the accurate identification and efficient development of shale oil resources [40]. To address this limitation, this study investigates the Qingshankou Formation shale succession in the Qijia–Gulong Sag of the Songliao Basin. Organic geochemical analyses, reservoir petrophysical measurements, and pore-throat characterization experiments are integrated to systematically characterize the organic matter abundance, thermal maturity, and hydrocarbon generation and expulsion capacity of the source rocks, together with the storage and flow properties of the sandstone interbeds [41]. Conventional core analyses and statistical methods are first applied to establish cutoffs for the porosity, permeability, and pore-throat parameters of the sandstone interbeds. Subsequently, given the near-source accumulation characteristics of shale oil, a source–reservoir-coupled approach is developed by integrating the source–reservoir spatial configuration, the hydrocarbon generation and expulsion capacity of the source rocks, and the storage and flow capacity of the sandstone reservoirs [42,43]. The conventional and source–reservoir-coupled approaches are then applied to representative wells spanning different productivity classes and validated against formation-test results. The source–reservoir coupling approach shows better agreement with observed well productivity and more effectively distinguishes among good-, moderate-, and poor-quality sandstone reservoirs. This approach provides a quantitative basis for effective reservoir identification, sweet spot interval selection, and resource assessment of interbedded shale oil systems in the study area while also helping to explain why their petrophysical cutoffs differ from those of conventional sandstone reservoirs.

2. Geological Settings

The Songliao Basin is located in northeastern China. The basin extends in a north–northeast direction with a total area of about 2.6×10^5 km^2. It is a large-scale Mesozoic and Cenozoic continental petroleum-bearing basin (Figure 1) [44–47]. The Songliao Basin began to form from the late Indosinian to the early Yanshanian period. The main development stage was from the middle to late Yanshanian period to the early Himalayan period. The late Himalayan period experienced compression and contraction, depositing Mesozoic and Cenozoic strata, and reached the peak of basin development in the Cretaceous [48]. The Songliao Basin has a dual structure of a lower fault and an upper depression in the vertical direction and has experienced three structural evolution stages: syn-rift stage, depression stage and structural inversion stage [49,50]. On the plane, it is divided into six first-level structural units: northern subduction area, northeast uplift area, southeast uplift area, central depression area, western slope area and southwest uplift area [50,51]. The

basin was in the rift stage from the Late Jurassic to the Early Cretaceous; it turned into the depression stage in the late Middle to Late Cretaceous, and depression sequences such as the Quantou Formation, Qingshankou Formation and Nenjiang Formation developed successively. The northern part of the basin is a key demonstration area for shale oil exploration and development. Medium- to high-maturity shale oil is mainly developed in the Qingshankou Formation, and transgression events occurred during the deposition process [52–54]. The Upper Cretaceous of the Songliao Basin is dominated by large continental freshwater lake basin sediments, with delta, semi-deep lake and deep lake sediments developing [46]. The Qingshankou Formation can be divided into three sections, and its sedimentary evolution manifests itself as a transition from lacustrine transgression to lacustrine regression [55]. The first member of the Qingshankou Formation (k_2qn_1) experienced lacustrine transgression, forming a huge semi-deep lake to deep lacustrine mud shale, dominated by pure shale-type shale oil [56]; the thickness of the dark mud shale of the second member of the Qingshankou Formation is greater than that of the first member of the Qingshankou Formation [57]. Then, the lake basin shrank, and the delta complex advanced into the basin. The delta front facies of the second member of the Qingshankou Formation (k_2qn_2) and the third member of the Qingshankou Formation (k_2qn_3) were dominated by intercalated shale oil [58]. The main research object in this study is the interlayered shale oil in the Qingshankou Formation in the Qijia–Gulong area.

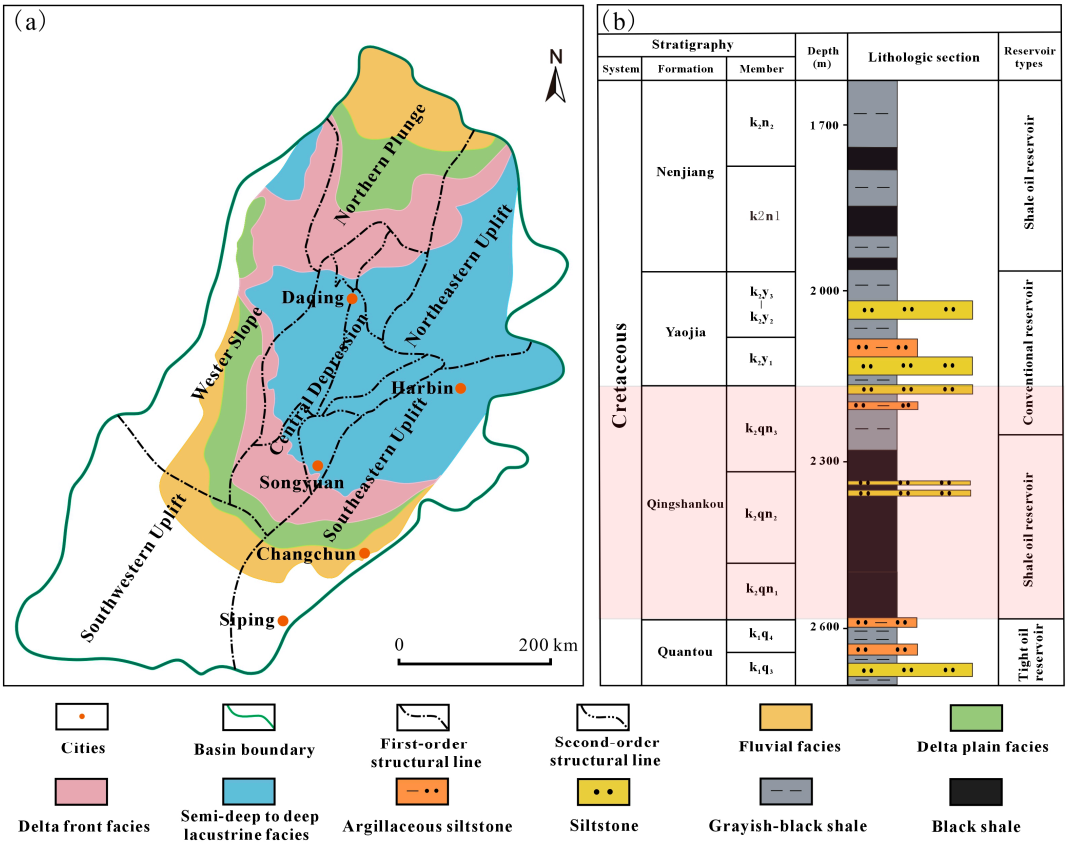


Figure 1. Regional geological overview map of Songliao Basin [59–61]. (**a**) Tectonic units and sedimentary facies; (**b**) generalized stratigraphic column.

3. Theory and Methods

Samples were collected from 16 wells. The dataset mainly comprised source rock organic geochemical analyses, reservoir petrophysical measurements, and oil-testing and production-test data, which were used to characterize the source rocks and reservoirs. Detailed information is provided in Table 1.

Table 1. Summary of the analytical methods, standards, instruments, experimental conditions, and sample allocation.

Experiment	Standard	Instruments and Equipment	Experimental Conditions	Wells Sampled	Formation	Sedimentary Facies
TOC determination	GB/T 19145-2022 [62]	CS-230 carbon–sulfur analyzer (LECO Corporation, St. Joseph, MI, USA)	Room temperature	Wells A, B, C, and D	Qingshankou	Semi-deep to deep lacustrine facies
Rock-Eval pyrolysis	GB/T 18602-2012 [63]	Rock–Eval 6 Plus pyrolysis analyzer (Vinci Technologies, Nanterre, France)	Room temperature	Wells A, B, C, and D	Qingshankou	Semi-deep to deep lacustrine facies
Kerogen-type	SY/T 5125-1996 [64]	Leica DMLD transmitted light and fluorescence microscopy system (Leica Microsystems GmbH, Wetzlar, Germany)	Room temperature	Wells A, B, C, and D	Qingshankou	Semi-deep to deep lacustrine facies
Ro measurement	SY/T 5124-2012 [65]	DM4500P microscope (Leica Microsystems GmbH, Wetzlar, Germany) equipped with an ODI302 microspectrophotometer (CRAIC Technologies, Inc., San Dimas, CA, USA)	23 ± 3 °C; relative humidity < 70%	Wells A, B, C, and D	Qingshankou	Semi-deep to deep lacustrine facies
Laser confocal	SY/T 7773-2024 [66]	Confocal laser scanning microscope(Leica Microsystems GmbH, Wetzlar, Germany)	Low-temperature, light-protected conditions under a dry nitrogen atmosphere	Wells B and E	Qingshankou	Semi-deep to deep lacustrine facies
MICP	GB/T 29171-2023 [67]	AutoPore IV 9505 mercury porosimeter (Micromeritics Instrument Corporation, Norcross, GA, USA)	Maximum mercury injection pressure of approximately 200.30 MPa	Wells A, B, C, D, and P	Qingshankou	Semi-deep to deep lacustrine facies
Thin section	SY/T 5368–2016 [68]	Axio Imager D1 (Carl Zeiss Microscopy GmbH, Jena, Germany), DM4500P(Leica Microsystems GmbH, Wetzlar, Germany)	Room temperature	Wells B, D, E, F, G, H, I, and J	Qingshankou	Semi-deep to deep lacustrine facies
SEM	SY/T 5162-2021 [69]	TESCAN VEGA GMS scanning electron microscope(TESCAN, Brno, Czech Republic)	20 °C; 40% relative humidity	Wells C, K, and P	Qingshankou	Semi-deep to deep lacustrine facies

Physical property	GB/T 29172-2012 [70]	ECK-II/IIIandAP-121(Nantong Feiyu Petroleum Technology Development Co., Ltd., Nantong, China), SMP-200(Core Laboratories L.P., Houston, TX, USA), NDP 605(Coretest Systems Inc., Morgan Hill, CA, USA), and CMS 300(Core Laboratories L.P., Houston, TX, USA)	23–25 °C; 47–50% relative humidity	Wells E, L, M, N, O, and P	Qingshankou	Semi-deep to deep lacustrine facies

3.1. Total Organic Carbon (TOC) Determination Experiment

Inorganic carbon was removed using dilute hydrochloric acid. After washing and drying, the TOC content was measured by high-temperature combustion coupled with infrared detection. TOC reflects the abundance of organic matter in rocks and is an important parameter for evaluating the basis of hydrocarbon generation in source rocks [71,72].

3.2. Rock-Eval Pyrolysis

The crushed rock samples were placed in a rock pyrolysis instrument, and the temperature was gradually raised according to the set program in an inert environment. The free hydrocarbon content S_1, kerogen thermal cracking hydrocarbon content S_2, carbon dioxide production S_3, and maximum pyrolysis peak temperature T_{max} were measured. Experimental results can be used to evaluate the hydrocarbon generation potential, organic matter type and thermal evolution degree of rocks [73]. Rock-Eval analysis was performed using a Rock–Eval 6 Plus analyzer in accordance with GB/T 18602-2012 [63]. The powdered samples were held at 300 °C for 3 min under an inert atmosphere to determine S_1 and were subsequently heated to 650 °C at 25 °C min^{-1} to determine S_2 and Tmax. S_3, hydrogen index (HI), and oxygen index (OI) values were subsequently calculated. The instrument was calibrated using a certified rock pyrolysis reference material, with blanks and reference samples included for quality control.

3.3. Kerogen Type

Kerogen was isolated and concentrated after acid treatment, and polished kerogen mounts were prepared. The morphology, color, and fluorescence of organic macerals were examined under transmitted light and fluorescence illumination. The proportions of inertinite, chitinite, vitrinite, and sapropelinite were counted to determine organic matter type, provenance, and hydrocarbon generation tendency.

3.4. Vitrinite Reflectance (R_o) Measurement Experiment

The separated kerogen was made into polished light sheets, and the reflectance of vitrinite particles was measured using a microscope photometer under oil immersion conditions. The average vitrinite reflectance R_o was obtained through multiple effective measurement points, which was used to evaluate the thermal maturity of organic matter.

3.5. Laser Confocal Experiment

Representative fresh core samples were selected, cut and surface-treated under low-temperature conditions to reduce the volatilization of light hydrocarbons and the redistribution of crude oil during the sample preparation process. A laser scanning confocal microscope was used to carry out reflected light–fluorescence combined scanning on the sample. Based on the differences in fluorescence responses of the crude oil components under different excitation and receiving bands, the location of oil substances in intergranular pores, intragranular pores and micro-cracks was identified. Continuous *Z*-axis optical sections were acquired and reconstructed in three dimensions to characterize oil distribution and quantify the oil-bearing area, fluorescence intensity, and occurrence modes.

3.6. Mercury Injection Capillary Pressure (MICP)

A dry rock sample was placed in a mercury porosimeter, and the external pressure was gradually increased so that the non-wetting phase mercury entered the pore throats of different sizes in sequence. Capillary pressure curves were constructed from the relationship between mercury intrusion pressure and intrusion volume. These curves were used to calculate displacement pressure, median pressure, pore-throat radii, pore-throat size distribution, and sorting parameters [74]. Based on this experimental analysis, the pore-throat structure and reservoir performance of the sandstone reservoir were obtained. MICP measurements were conducted using an AutoPore IV 9505 mercury porosimeter in accordance with GB/T 29171-2023 [67]. Samples dried to a constant mass were evacuated before stepwise mercury intrusion and extrusion measurements. The maximum intrusion pressure was approximately 200.30 MPa. Equivalent pore-throat sizes were calculated using the Washburn equation, with a mercury surface tension of 0.485 N m^{-1} and a contact angle of 130°.

3.7. Thin Section

A rock sample was evacuated and then injected with colored epoxy resin to fill the connected pores with the resin. After solidification, it was cut and ground into cast thin slices. Mineral composition, grain structure, cement, diagenesis and pore type were observed under a polarizing microscope. Colored resins can highlight intergranular pores, intragranular dissolved pores, mold pores and micro-cracks and enable semi-quantitative evaluation of reservoir space through porosity statistics.

3.8. Scanning Electron Microscope (SEM)

SEM images were acquired by rastering a focused electron beam across the sample surface and detecting the resulting secondary electron and backscattered electron signals. This bombarded the sample surface point by point in a raster-like scanning manner to excite electronic signals of different depths, which were synchronously transmitted to a computer display through an amplifier to form a real-time imaging record [75]. Combined with secondary electron, backscattered electron and energy spectrum analysis, pore type, clay mineral occurrence mode, mineral dissolution, cementation and micro-crack characteristics were identified. The scanning electron microscope had high spatial resolution, but the observation range was small, so attention was paid to the representativeness of the field of view.

3.9. Physical Property Experiments

Regular plunger samples were drilled from a full-diameter core, the sampling direction and depth were recorded, and the porosity and permeability were measured after oil washing, salt washing and drying. Porosity is usually measured by the helium expansion

method, and permeability is generally measured by the steady-state gas measurement method; for dense samples, the pulse attenuation method can be used. The experiment mainly obtains parameters such as porosity, gas permeability, particle density and bulk density, which are the basic data for determining the lower limit of reservoir physical properties. Core porosity and permeability were measured in accordance with GB/T 29172-2012 [70]. The samples were cleaned, dried to a constant mass, and cooled to room temperature before analysis using ECK-II/III, AP-121, SMP-200, NDP 605, and CMS 300 instruments. Measurements were performed at 23–25 °C and 47–50% relative humidity. Instrument calibration and leak testing were conducted before analysis, and the results were recorded after the pressure and flow readings had stabilized.

In summary, this study establishes a comprehensive multiscale experimental characterization system targeting interbedded sandstone reservoirs in shale. The system integrates three core modules: source rock organic geochemical testing, reservoir microscopic pore-throat characterization, and macroscopic petrophysical measurement.

Specifically, TOC analysis, Rock-Eval pyrolysis, kerogen maceral identification, and R_o testing quantitatively characterized the accumulation, type and thermal maturity of organic matter in source rocks. This provides a geochemical basis for clarifying source–reservoir configuration relationships and hydrocarbon supply capacity. Thin-section analysis, SEM, laser scanning confocal microscopy, and MICP provided multiscale characterization of mineral composition, diagenetic features, pore-throat distribution, and oil occurrence, thereby revealing the microscopic controls on reservoir quality heterogeneity. Core-based petrophysical tests directly delivered porosity and permeability parameters, which served as the fundamental dataset for determining the lower petrophysical limits of effective reservoirs.

Quality assurance and quality control procedures were implemented according to the corresponding analytical standards and laboratory protocols. Instrument performance was checked using appropriate reference materials before sample analysis. Where replicate measurements were available, analytical uncertainty was expressed as the standard deviation or relative deviation of replicate results.

Within this established experimental framework, the methodological refinement of the present study is to link measured source rock and reservoir parameters to source–reservoir coupling categories and derive coupling-specific petrophysical cutoffs. This approach provides a geologically constrained complement to conventional cutoff evaluation. It also helps clarify why petrophysical cutoffs differ between interbedded shale oil reservoirs and conventional sandstone reservoirs.

3.10. Determination of the Source–Reservoir Pressure Difference

Formation pressure was obtained from the existing one-dimensional geomechanical well-log interpretation. A continuous formation pressure curve was calculated using the equivalent depth method rather than measured directly by MDT or RFT. For each tested interval, the representative pressures of the adjacent source rock and sandstone reservoir were defined as the median values of the interpreted pressure curve within the corresponding depth intervals. To eliminate the hydrostatic pressure difference caused by unequal burial depths, excess pressure was calculated as:

$$P_{ex} = P_P - \rho_w g H \quad (1)$$

where P_P is the interpreted formation pressure, ρ_w is formation water density, g is gravitational acceleration, and H is true vertical depth. The source–reservoir pressure difference was then calculated as:

$$\Delta P = P_{ex,s} - P_{ex,r} \quad (2)$$

where $P_{ex,s}$ and $P_{ex,r}$ are the excess pressures of the source rock and sandstone reservoir, respectively. A positive ΔP represents a pressure potential favorable for hydrocarbon migration from the source rock to the reservoir. Because the pressure profile was derived from well-log interpretation rather than direct pressure measurements, ΔP is treated as a relative pressure-driving indicator specific to the study area.

4. Results

4.1. Characteristics of Source Rocks

4.1.1. The Hydrocarbon Quality

The organic matter abundance characteristics of intercalated shale oil source rocks in the Qingshankou Formation in the Songliao Basin were comprehensively evaluated based on the intersection relationship between TOC and $S_1 + S_2$ (Figure 2). The samples come from wells A, B, C and D. The overall data are mainly distributed in the medium–good source rock evaluation interval, and some samples reach the level of high-quality source rock. The TOC content is generally high, and the TOC of most samples exceeds the evaluation threshold, indicating that the source rocks in the study area have better organic matter enrichment conditions [76]. The overall distribution of $S_1 + S_2$ values is broad, but most samples are in a higher range, and some samples show significant high hydrocarbon generation potential characteristics. There is a certain positive correlation between TOC and $S_1 + S_2$, indicating that as the abundance of organic matter increases, its hydrocarbon generation potential increases as a whole, reflecting that the abundance of organic matter is a key geochemical parameter that controls the hydrocarbon generation capacity of the source rock in the study area [48]. There are certain differences in the organic matter abundance of source rocks between different wells. Among them, the A, C and D samples are mainly distributed in the good–high-quality source rock interval, showing relatively stable high abundance characteristics. The B sample has a relatively wide distribution range, with medium- to high-quality source rocks developed, indicating that the source rocks in the study area have certain heterogeneity both vertically and horizontally. Generally speaking, the Qingshankou Formation source rock has high organic matter abundance and good hydrocarbon generation potential, which provide an important material basis for the formation of intercalated shale oil.

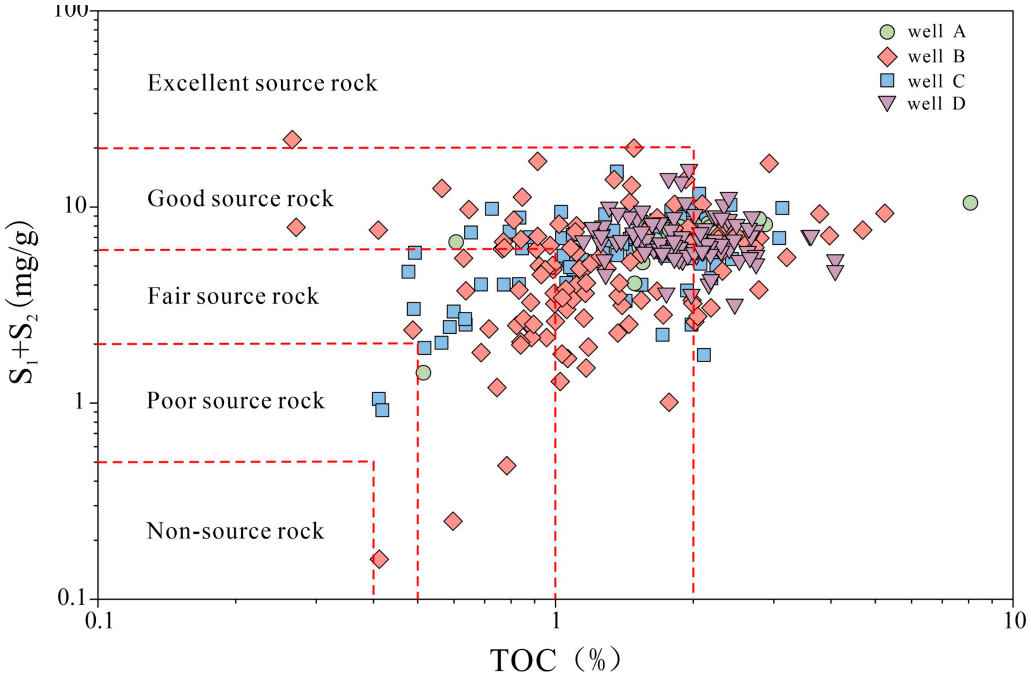


Figure 2. Organic matter abundance chart of interlayered shale oil source rocks.

4.1.2. Types of Organic Matter

Based on the statistical analysis results of samples from different wells (Figure 3), the organic matter type of the interlayered shale oil source rock in the Qingshankou Formation in the study area is mainly type I kerogen, with type II_1 organic matter locally developed. The overall organic matter combination shows typical oil-generating organic matter characteristics. Judging from the comparison results between wells, the samples from wells A, B, C and D are all dominated by type I organic matter, with well C accounting for the highest proportion of type I organic matter. Wells A and B also show obvious type I dominant characteristics. Type II_1 organic matter has developed in some well sections, among which well B has a relatively significant proportion, but the overall proportion is low. The above results show that the source rock in the study area was in a relatively reducing depositional environment during the deposition period, which was conducive to the preservation and enrichment of hydrogen-rich organic matter (such as algae organic matter), thus forming an organic matter combination type dominated by type I–type II_1. Taken together, the organic matter type of the Qingshankou Formation source rock is generally superior and has typical oil-generating kerogen assemblage characteristics. Combined with the aforementioned analysis of organic matter abundance and thermal evolution characteristics, the source rocks in the study area not only have a good material foundation [77] but are also in a suitable thermal evolution stage, providing favorable geochemical conditions for the formation and enrichment of intercalated shale oil.

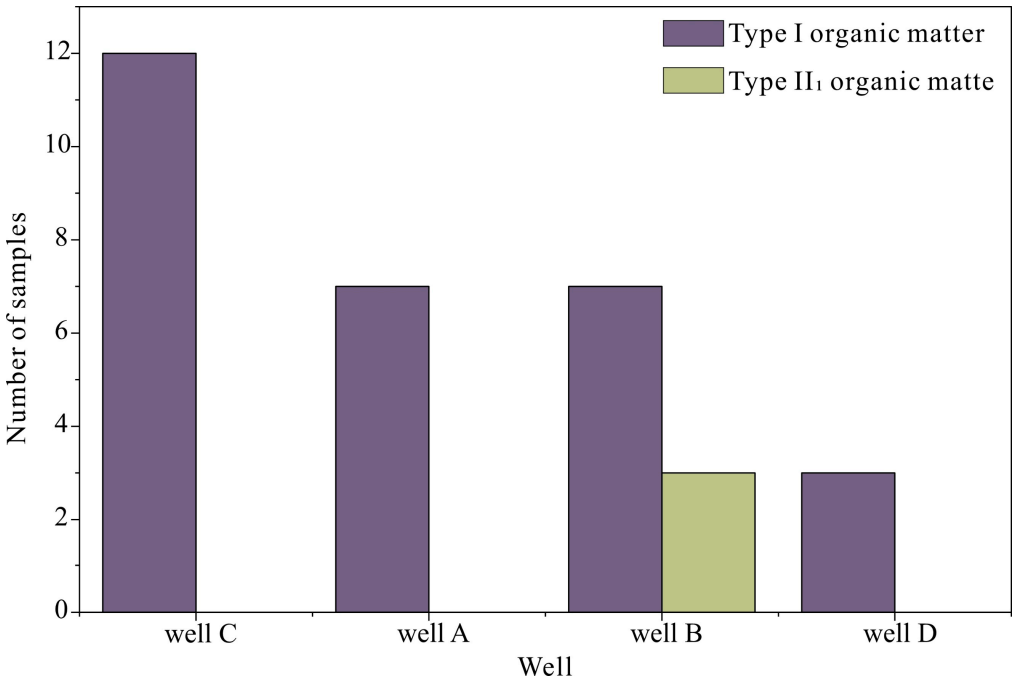


Figure 3. Chart of organic matter types of interlayered shale oil source rocks.

4.1.3. Organic Matter Maturity

Vitrinite reflectance (R_o) is a key indicator for evaluating the thermal evolution degree and organic matter maturity of hydrocarbon source rocks and can effectively indicate the evolution characteristics of their hydrocarbon generation stages [78]. The R_o value of the Qingshankou Formation source rock in the study area is mainly distributed between 0.5% and 1.5% (Figure 4a) and is generally in the mature stage, indicating that the source rock has entered the effective oil generation window and has the thermal evolution conditions to generate liquid hydrocarbons [79,80]. As the burial depth increases, the R_o value

generally shows a gradually increasing trend, suggesting that the degree of thermal evolution is significantly controlled by burial, consistent with the general evolution law of organic matter maturity in sedimentary basins that increases with burial depth. There are certain spatial differences in R_o values between different wells. Among them, wells B and C show high R_o values in relatively shallow sections, indicating that their local thermal evolution is relatively high. Samples from wells A and D are mainly distributed in deeper sections, and their R_o values are overall higher, indicating that the degree of thermal evolution of source rocks is further enhanced under stronger burial conditions. In general, the thermal evolution degree of the Qingshankou Formation source rock in the study area is mainly in the mature stage, and the overall oil generation window is within the range of a stable oil generation window, which provides favorable thermal evolution conditions for the continuous generation and enrichment of shale oil.

The pyrolysis parameter T_{max} is one of the important indicators for evaluating the degree of thermal evolution of hydrocarbon source rocks. It is often used in combination with vitrinite reflectance (R_o) to describe the maturity of organic matter and the stage of hydrocarbon generation evolution. The T_{max} value of the Qingshankou Formation source rock in the study area is mainly distributed between 430 °C and 470 °C (Figure 4b), which overall indicates that the source rock is in the mature stage, suggesting that it has entered the effective oil generation window and has the thermal evolution conditions to form liquid hydrocarbons. This result is consistent with the R_o analysis, further verifying the reliability of the source rock maturity evaluation results in the study area. Judging from the vertical distribution characteristics, the T_{max} value generally shows a gradually increasing trend with the increase in burial depth, indicating that the degree of thermal evolution is significantly controlled by burial, consistent with the general law that the thermal evolution of organic matter in sedimentary basins increases with burial depth. There are certain differences in T_{max} values between different wells. Among them, the samples from wells B and C are mainly distributed in the depth range of about 2000 to 2300 m, and the T_{max} value is generally in the mature stage. In contrast, the burial depth of the samples from wells A and D is relatively large, and the corresponding T_{max} value is generally high, suggesting that the degree of thermal evolution of organic matter is further enhanced under stronger burial conditions. Overall, the T_{max} characteristics of the Qingshankou Formation source rock and the R_o results corroborate each other, indicating that the source rock in the study area is in the mature oil generation stage as a whole and has the ability to continuously generate hydrocarbons, providing favorable thermal evolution conditions for the formation and enrichment of intercalated shale oil.

Comprehensive analysis of geochemical parameters such as TOC, R_o, T_{max}, and organic matter types shows that the intercalated shale oil source rock of the Qingshankou Formation in the Songliao Basin is characterized by high organic matter abundance, superior organic matter types, and moderate thermal evolution. The TOC evaluation results show that the source rock in the study area as a whole reaches the standard of medium–good source rock, and some samples can reach the level of high-quality source rock, indicating that it has good organic matter enrichment conditions and material foundation. The results of the thermal evolution parameters (R_o and T_{max}) consistently indicate that the source rock is in a mature stage as a whole, has entered the effective oil generation window, and has the thermal evolution conditions to form liquid hydrocarbons. The types of organic matter are mainly type I–type II_1, indicating that the study area is dominated by hydrogen-rich oleogen and has good potential for liquid hydrocarbon generation.

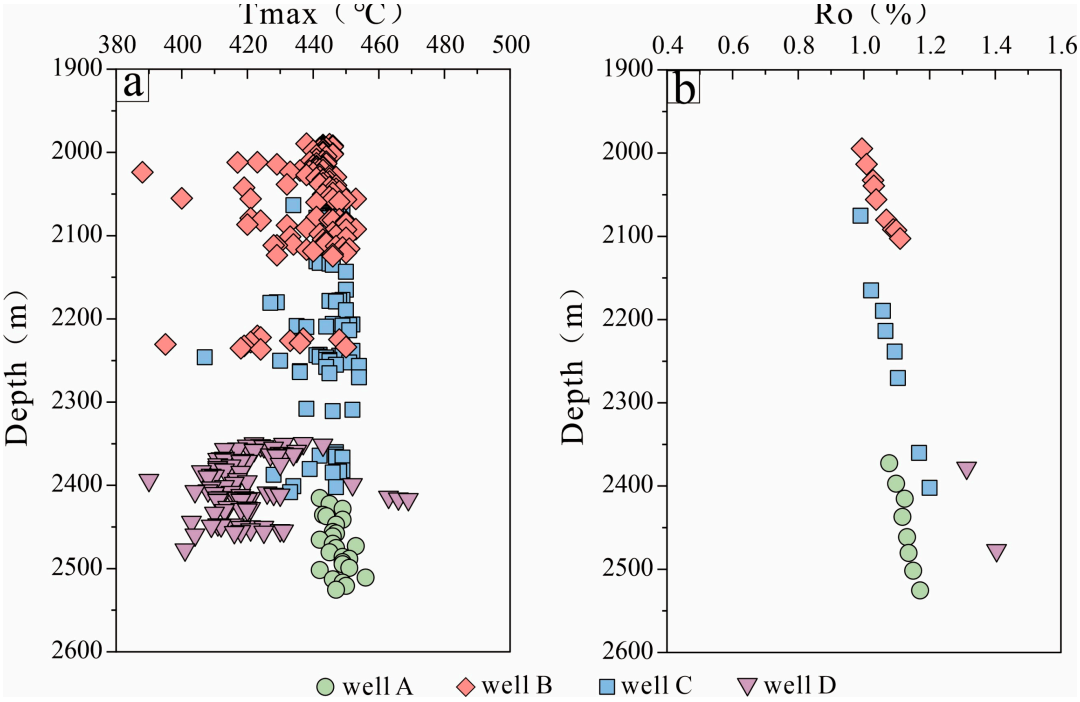


Figure 4. Organic matter maturity chart of interlayered shale oil source rocks. (**a**). Rock pyrolysis peak temperature. (**b**). Vitrinite reflectance.

Taken together, the overall quality of the intercalated shale oil source rock in the Qingshankou Formation is relatively good, and it has a good hydrocarbon generation foundation and resource potential. This set of source rocks can provide continuous oil source supply for the generation and enrichment of interlayered shale oil and is a key geological constraint for evaluating the shale oil exploration potential in the study area and establishing a source–reservoir combination model.

4.2. Characteristics of Sandstone Reservoirs

4.2.1. Petrology

Statistical analysis of thin-section petrographic data indicates that the sandstone interlayers of the Qingshankou Formation in the study area are predominantly very fine- to fine-grained and consist mainly of feldspathic litharenite, with subordinate lithic arkose. Regarding the overall performance, the lithic content is the highest, reaching an average of 40.2%, followed by the feldspar content, at about 32%, and the quartz content is the lowest, at about 25%, indicating that the sandstone skeleton particles are mainly composed of unstable components such as lithic debris and feldspar.

The Q-F-R triangular diagram of clastic components (Figure 5) shows that the sandstone reservoir is dominated by feldspathic clastic sandstone, and none of the samples entered the quartz sandstone and quartzite sandstone areas, further indicating that its quartz enrichment is low and its compositional maturity is generally low. The extensive preservation of feldspar and lithic debris indicates that the clastic materials experienced relatively limited chemical weathering and sedimentation recycling before deposition, which may reflect recent source supply and faster transport–deposition processes.

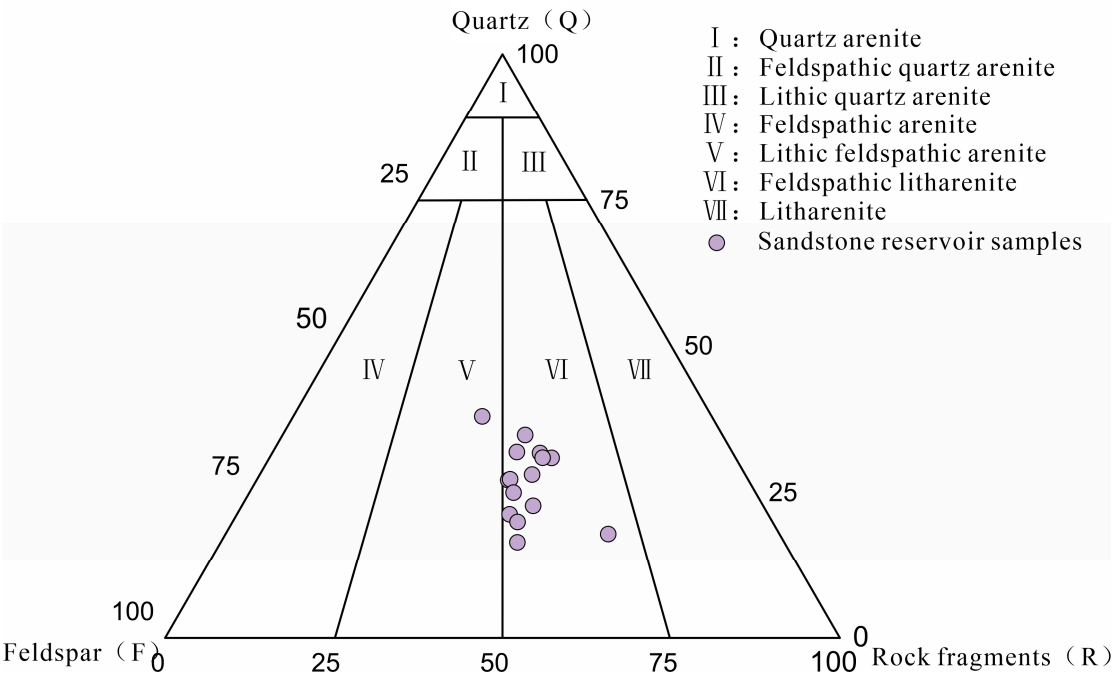


Figure 5. Q-F-R clastic component triangle diagram of the sandstone reservoir in the study area.

4.2.2. Reservoir Space

Understanding the shale oil reservoir space is very necessary for research [81]. Scanning electron microscopy and cast thin section observations show that the types of reservoir spaces in the sandstone interlayers in the study area are diverse, mainly including residual intergranular pores, secondary dissolved pores, biological cavity pores, mineral intercrystalline pores and matrix micropores. Pores of different origins are significantly different in scale, shape and connectivity, forming a composite storage space with intergranular pores and secondary dissolved pores as the main body and fine intergranular pores and matrix pores as the supplement.

Residual intergranular pores are more effective storage spaces in sandstone interlayers. In the cast thin section, the intergranular pores are blue, mainly distributed between quartz, feldspar and rock debris particles, and are mostly triangular, polygonal or irregular harbor-shaped (Figure 6a). These pores are relatively large in scale and well connected with each other and are the main spaces for free oil occurrence and seepage. Secondary dissolved pores mainly include intragranular dissolved pores and intergranular dissolved pores. Intragranular dissolved pores are mostly developed inside feldspar and unstable rock fragments, in the shape of spots, honeycombs or irregular bays; intergranular dissolved pores are mainly developed along the edges of particles, particle contact parts or early cement distribution areas (Figure 6b). The high contents of feldspar and lithic fragments provide abundant material susceptible to dissolution. Consequently, dissolution is an important constructive diagenetic process that improves sandstone storage capacity. Some samples have storage spaces related to bioclastics (Figure 6c). This type of pore may be formed by the preservation of original biological body cavities or the later dissolution of fillings in shells. Under the scanning electron microscope, fine intercrystalline pores can be seen between the spherical mineral aggregates and authigenic crystals (Figure 6d,e), and scattered point-like and elliptical micropores can also be seen inside the fine-grained matrix (Figure 6f).

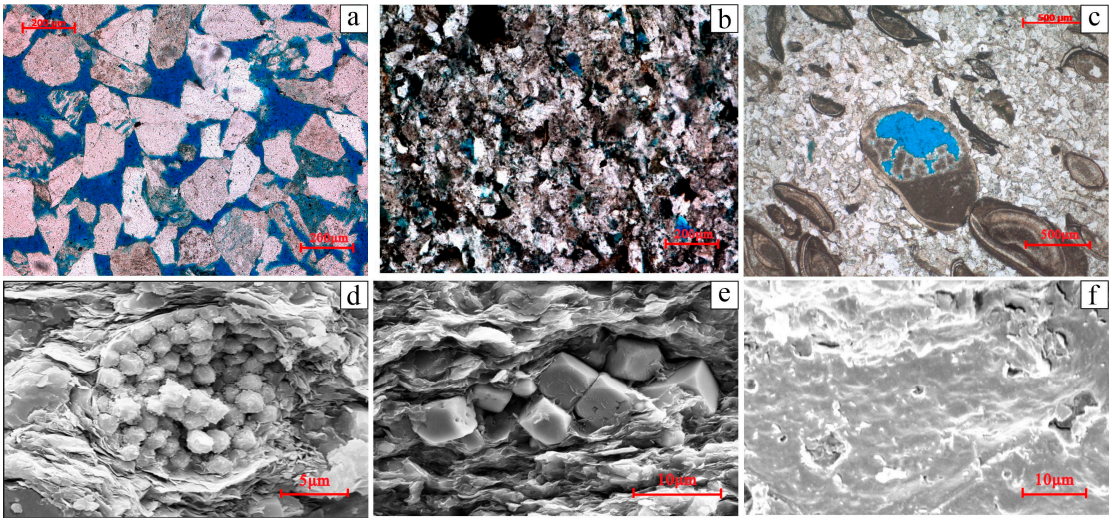


Figure 6. Reservoir space of an interlayered shale oil sandstone reservoir. (**a**). Intergranular pores. (**b**). Intergranular dissolved pores. (**c**). Biological cavity pores. (**d**). Intercrystalline pores. (**e**). Intercrystalline pores. (**f**). Matrix micropores.

In general, the sandstone interlayers in the study area have a reservoir space combination of "mainly residual intergranular pores and secondary dissolved pores, with partially developed biological cavity pores, supplemented by intercrystalline pores and matrix micropores". Compaction, clay mineral filling, and carbonate cementation resulted in the loss of primary intergranular pores, while the dissolution of feldspar, cuttings, and some cements caused secondary transformation of the pores. Intergranular pores and the dissolved pores connected with them constitute the main effective storage space, and the seepage contribution of isolated intragranular pores and fine intergranular pores is relatively limited. Therefore, the reservoir quality of sandstone interlayers not only depends on the degree of pore development but is also mainly controlled by the effective throat size and the connectivity between intergranular pores and dissolved pores.

4.2.3. Oil-Bearing Components

The results of microscopic component identification show that both light and heavy oil-bearing components are developed in the siltstone in the study area, but their contents and spatial distributions are obviously heterogeneous (Figure 7). The light component and heavy component contents of the 2040.27 m siltstone in well E are 0.24% and 0.28%, respectively. The oil-bearing components are mostly distributed in points, short strips and local clusters, with a total identified content of 0.52%. Biodetritus and intergranular pores are relatively developed in thin sections, and the locally preserved biocavity pores and intergranular pores provide favorable space for the filling and enrichment of oil (Figure 7a–c). In contrast, the light component and heavy component contents in the 2014.23 m siltstone in well B are only 0.07% and 0.10%, and the total identification content is 0.17%. It is mainly distributed in scattered fine points and irregular lines, and the scale and continuity of oil-bearing patches are weak (Figure 7d–f). Its finer particles, higher impurity or cement content, and poor intergranular pore preservation conditions may be important reasons for the low oil content.

The contents of heavy components are slightly higher than those of light components, indicating that the oil in the sandstone interlayer in the study area as a whole shows certain enrichment characteristics of heavy components. The total identified oil content of samples from well E is approximately 3.1 times that of samples from well B, reflecting significant differences in the oil content of sandstone interlayers in different well areas or sections. Generally speaking, the oil in the sandstone interlayer is mainly controlled by

effective intergranular pores, biological cavity pores and local dissolution pores; the oil-containing components are relatively concentrated in the parts with more developed pores and good connectivity, while the oil-containing components in the dense parts with high content of heterogeneous groups and cements are mainly dispersed. Therefore, the development degree and connectivity of the reservoir space are important factors that control the oil abundance and microdistribution of sandstone interlayers.

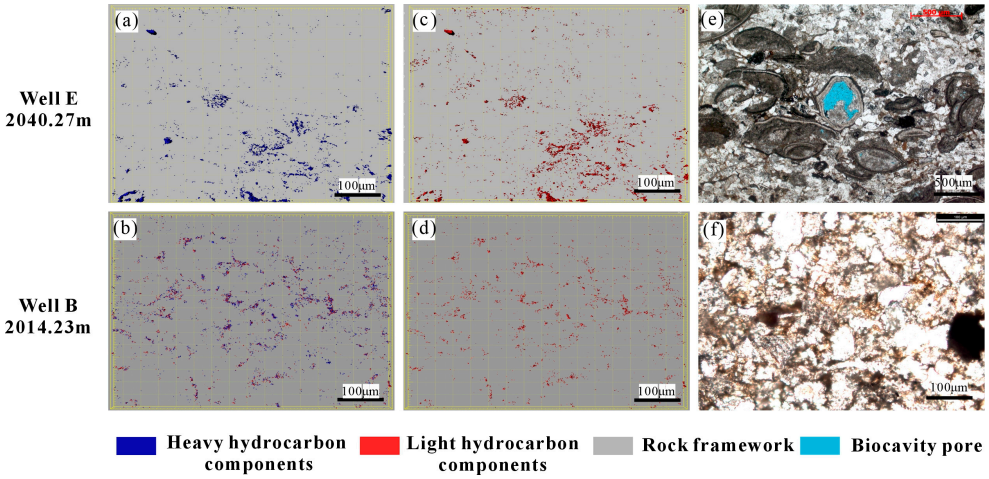


Figure 7. Oil-bearing characteristics of interlayered shale oil sandstone reservoirs. (**a**,**b**). Heavy hydrocarbon component distribution (**c**,**d**) Light hydrocarbon component distribution (**e**,**f**) Thin-section photomicrograph

4.3. Sandstone Reservoir Threshold According to Traditional Methods

4.3.1. Porosity and Permeability Intersection Method

Porosity and permeability characterize the storage capacity and seepage capacity of the reservoir, respectively, and the matching relationship between the two can be used to identify critical points where reservoir physical properties change significantly [82]. The porosity–permeability intersection relationship of 170 sandstone samples in the study area indicates that the permeability generally shows an exponential upward trend with the increase in porosity (Figure 8), and the fitting relationship is:

$$K = 0.0043e^{0.3839\varphi} \quad (3)$$

where K is permeability, mD; is porosity, %; and the fitting coefficient of determination R^2 = 0.4966.

When the porosity is low, the permeability of the sample is generally at a low level, and the change with porosity is small, indicating that the new pores are mainly fine pores with poor connectivity and the improvement in seepage capacity is limited. When the porosity approaches 8.0%, the increase in permeability increases significantly, indicating that the effective pores and connected throats begin to increase significantly, and the reservoir changes from an ineffective–low-efficiency state to an effective reservoir. According to the changing trend of the fitting curve and the distribution boundary of low-permeability samples, a porosity of 8.0% and a permeability of 0.09 mD were respectively used as the lower limits of reservoir physical properties determined by the porosity–permeability intersection method.

This method reflects the overall porosity–permeability relationship of the sandstone in the study area. Its fitting degree is moderate, indicating that in addition to being controlled by porosity, reservoir permeability is also significantly affected by throat size, cementation, mud content, and fracture development. Therefore, the lower limit determined

by the pore–permeability intersection method needs to be further verified using pore-throat structure and oil content data.

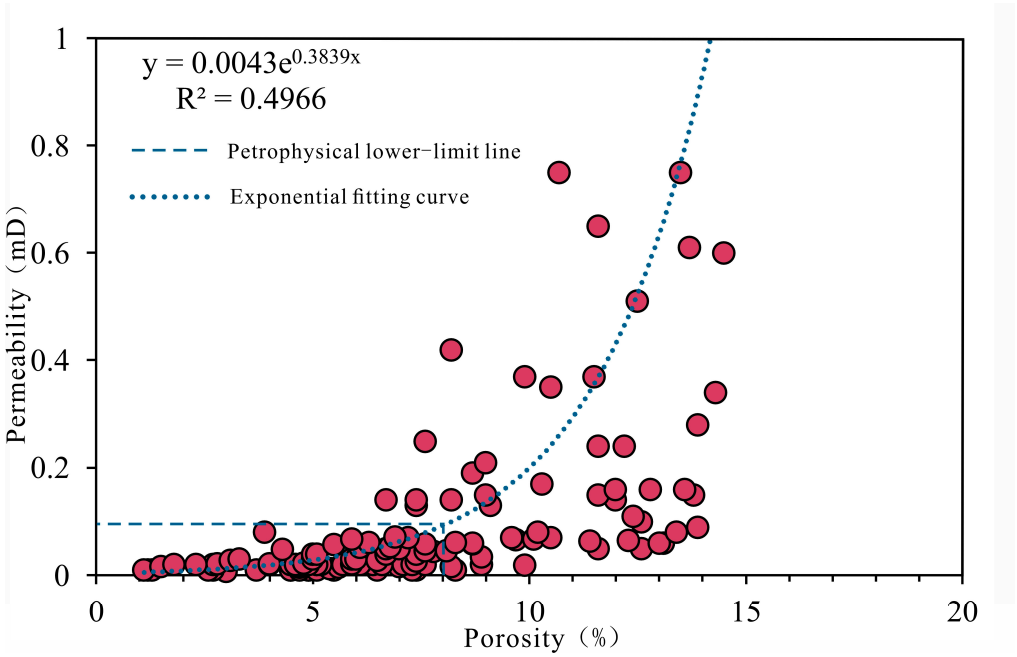


Figure 8. Results of the porosity and permeability intersection method showing the lower limit of reservoir physical properties.

4.3.2. Threshold Pressure Method According to the MICP Test

The displacement pressure is the capillary pressure that needs to be overcome when the non-wetting phase begins to enter the largest connected throat of the rock; it can be used to reflect the maximum effective throat size that controls fluid entry into the reservoir. A lower displacement pressure usually indicates that the maximum connected throat radius is larger and the pore-throat connectivity is better; an increase in displacement pressure indicates that the pore throats tend to become smaller and the resistance to fluid entry and migration increases.

The mercury injection experiment results of 16 sandstone samples from the study area show that the displacement pressure has a significant negative correlation with porosity and permeability (Figure 9). As the displacement pressure increases, the porosity decreases overall and the permeability decreases more significantly. When the displacement pressure is low, the porosity and permeability of the sample are high overall, indicating that there are relatively large effective throats in the reservoir; when the displacement pressure increases to about 1.3 MPa, the porosity and permeability enter the low-value range, indicating that the pore-throat size is significantly reduced and the effective seepage capacity of the reservoir rapidly deteriorates.

The displacement pressure–porosity and displacement pressure–permeability relationship diagrams show the fitted changing trends of high and low physical property samples, respectively. The turning position of the two trend lines corresponds to a porosity of approximately 8.0% and a permeability of approximately 0.11 mD. This result is basically consistent with the porosity and permeability intersection method, indicating that when the physical properties are lower than this critical value, the maximum connected throat of the reservoir becomes significantly thinner, the capillary entry pressure increases, and the oil and gas charging and seepage conditions are significantly restricted. Therefore, the lower limits of physical properties determined by the mercury injection displacement pressure method are a porosity of 8.0% and a permeability of 0.11 mD.

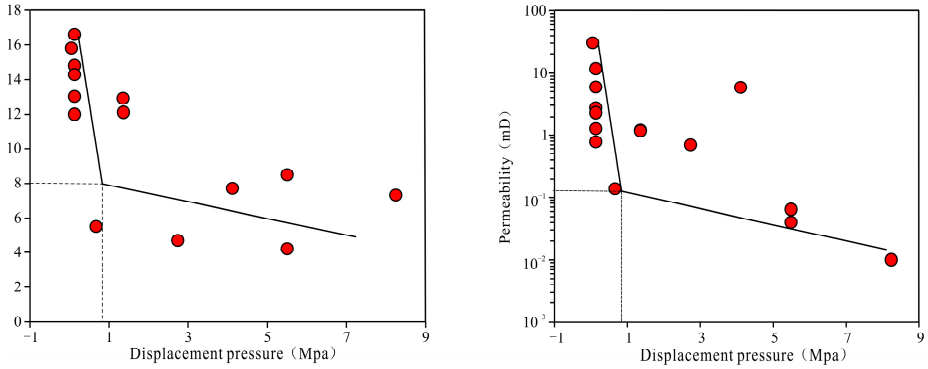


Figure 9. Results of the mercury injection displacement pressure method showing the lower limit of reservoir physical properties.

4.3.3. Minimum Pore-Throat Radius Method

Pore throats are key channels that connect different pores and control fluid migration. When the throat radius reaches a certain scale, oil and gas can overcome capillary resistance and enter the reservoir under formation conditions and migrate effectively. Existing experimental studies have shown that when the pore-throat radius of a sandstone reservoir is less than 0.1 μm, the capillary pressure required for oil and gas to enter the pore system increases significantly, making it difficult to form effective oil and gas charging and accumulation. Therefore, 0.1 μm can be used as the critical pore-throat radius of an effective reservoir [29,31]. There is a good exponential positive correlation between the sandstone permeability and the median pore-throat radius in the study area (Figure 10), and the fitting relationship is:

$$K = 0.0819e^{6.497r} \quad (4)$$

where K is the permeability, mD; r is the median pore-throat radius, μm; and the fitting determination coefficient $R^2 = 0.8196$. The high coefficient of determination indicates that the pore-throat radius is the key factor controlling the permeability of sandstone in the study area.

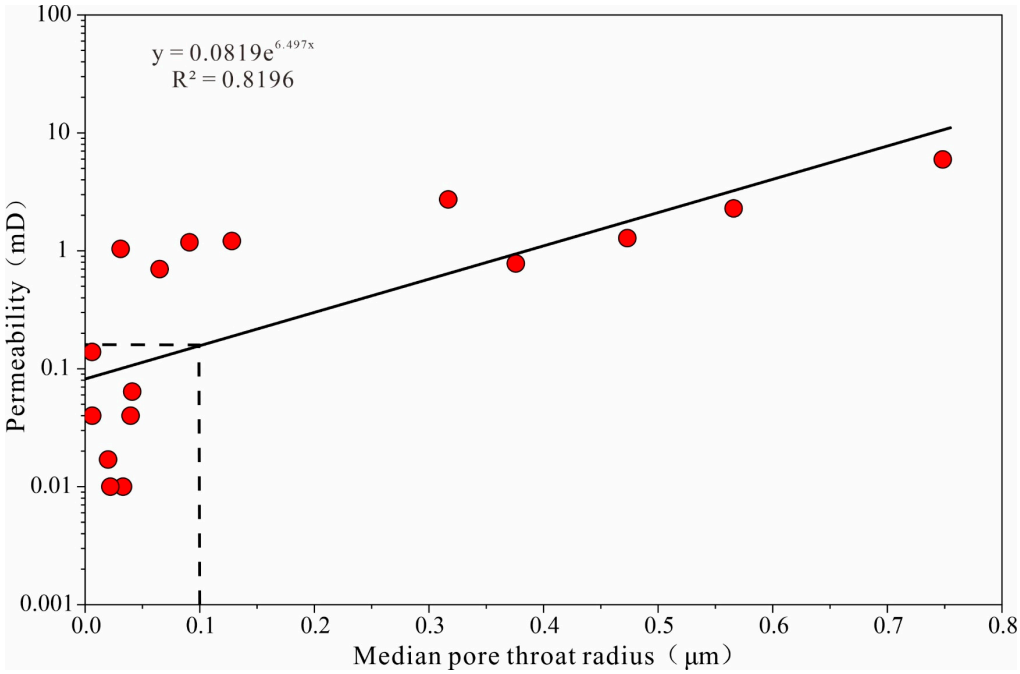


Figure 10. Minimum pore-throat radius method to determine the lower limit of reservoir physical properties.

Substituting the critical pore-throat radius of 0.1 μm into the fitting relationship, the corresponding permeability is calculated to be approximately 0.16 mD. Further combining the corresponding relationship between porosity and pore-throat structure, the lower limit of porosity is approximately 8.8%. This result is slightly higher than the lower limit determined by the pore–permeability intersection method and the threshold pressure method, mainly because the minimum pore-throat radius method emphasizes the pore-throat conditions required for oil and gas to effectively enter and migrate, and the discrimination standard is relatively strict. At the same time, the median pore-throat radius reflects the overall characteristics of the pore-throat system, which has different physical meanings from the displacement pressure controlled by the maximum connected throat.

4.3.4. Oil Occurrence State Method

Oil occurrence directly records the combined effects of hydrocarbon charging, reservoir space availability, and pore-throat connectivity [83]. Based on core and thin section observations, the oil occurrence of the sandstone in the study area was divided into oil immersion, oil spots, oil traces and no indication grades, and cross-analysis was carried out with porosity and permeability.

The results show that there is an overall positive correlation between the oil content grade and the physical properties of sandstone (Figure 11). Non-display samples are mainly distributed in low-porosity and low-permeability areas, with porosity less than 8.0% and permeability below 0.08 mD. As porosity and permeability increase, the oil level of the samples gradually changes from no display to oil stains, oil spots and oil immersion. When the porosity reaches 8.0% and the permeability reaches 0.08 mD, the oil content increases significantly, indicating that the sandstone begins to have more effective oil and gas charging and preservation conditions.

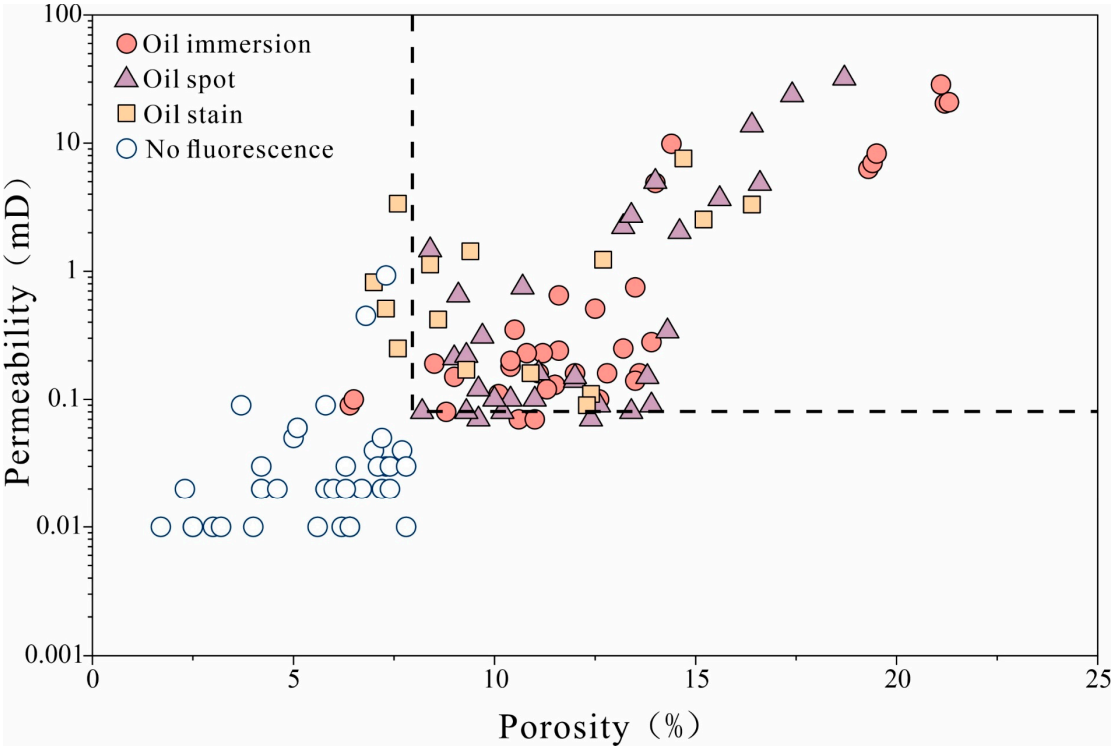


Figure 11. The lower limit of reservoir physical properties without the oil occurrence method.

5. Discussion

5.1. Source–Reservoir Assemblage

In interlayered shale oil, the sandstone interlayer is not only the main reservoir unit for enrichment of organic matter but also an important charging target after short-distance migration of oil and gas generated from shale. Compared with conventional oil reservoirs, this type of oil reservoir usually lacks long-distance migration processes, and its accumulation efficiency is controlled by the spatial configuration relationship between source rocks and sandstone reservoirs [47,84]. Therefore, source–reservoir configuration encompasses the vertical stacking of source rocks and sandstone interlayers, hydrocarbon supply capacity, source–reservoir contact, migration distance, pressure difference, and sandstone petrophysical properties. Evaluating petrophysical cutoffs under different source–reservoir configurations provides a geologically conditioned complement to conventional experimental and empirical methods.

Based on the vertical stacking relationship, contact degree and hydrocarbon supply direction between source rocks and sandstone interlayers, the interlayered shale oil source and reservoir configuration in the study area can be divided into three basic types: source interlayer type, source–reservoir interlayer type and reservoir interlayer source type (Figure 12).

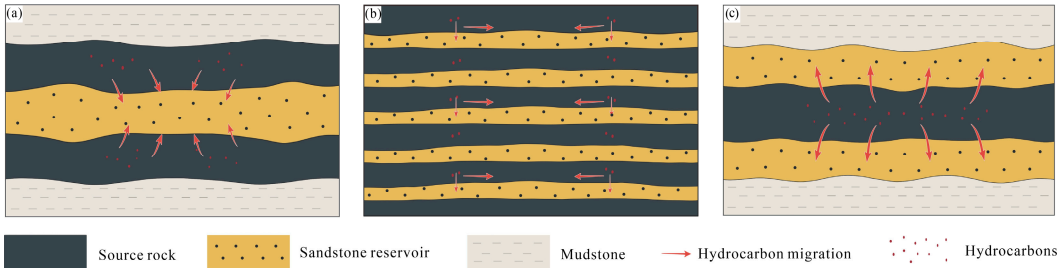


Figure 12. Schematic diagram of the source–storage configuration relationship. (**a**). Source sandwiched with reservoir type. (**b**). Source with reservoir interlayered type. (**c**). Storage sandwiched with source type.

(1) Source clamp reservoir type**.**

The source–reservoir type shows that the sandstone reservoir is located between two sets of effective source rocks, and both the upper and lower source rocks can supply hydrocarbons to the middle sandstone interlayer. In this type, the sandstone is in direct contact with the source rock and has the characteristics of bidirectional hydrocarbon supply, large source–reservoir contact area, and short migration distance (Figure 12a).

During the hydrocarbon generation process, the oil and gas produced by the upper and lower source rocks can migrate to the sandstone interlayer, driven by pressure. When the source rocks on both sides have strong hydrocarbon supply capacity, the sandstone pore-throat conditions are good, and the source–reservoir pressure difference is enough to overcome the capillary resistance, the sandstone can be fully charged. Therefore, the source–reservoir type usually has higher accumulation efficiency and is one of the most favorable source–reservoir configurations for interlayered shale oil.

(2) Source–reservoir interlayer type**.**

The source–reservoir interbed type consists of multiple sets of thin-layered source rocks and sandstone interlayers that frequently alternate. This type has the characteristics of frequent source–reservoir contact, large contact area, short migration path, and co-charging of multiple layers (Figure 12b). Hydrocarbons can enter the sandstone thin layer vertically and laterally from adjacent source rocks, thus forming a multilayered, dispersed oil-bearing combination.

The source–reservoir interbedded configuration generally favors efficient hydrocarbon supply. However, the oil content of individual sandstone interlayers also depends on layer thickness, lateral continuity, pore-throat structure, and the quality of adjacent source rocks. The reservoir-sandwiched-source configuration is more sensitive to source rock hydrocarbon supply capacity, the source–reservoir pressure difference, and the petrophysical properties of the upper and lower sandstone intervals.

(3) Reservoir clamp source type**.**

The reservoir interface source type shows that the effective source rock is located between the upper and lower sets of sandstone reservoirs, and oil and gas migrate from the central source rock to the sandstones on both sides (Figure 12c). This type can still form a two-way hydrocarbon supply, but the same set of source rocks needs to distribute oil and gas to the upper and lower sandstone layers at the same time. The amount of hydrocarbon supply obtained per unit of sandstone may be lower than that of the source sandwich type.

When the thickness of the upper and lower sandstones is large, or the scale of the reservoir space significantly exceeds the hydrocarbon supply capacity of the source rock, insufficient hydrocarbon supply and uneven charging are likely to occur. At the same time, water layers or inefficient layers may develop inside the sandstone layer, leading to oil–water differentiation and productivity differences. Therefore, the effectiveness of the source–reservoir type is more dependent on the hydrocarbon supply intensity of the source rock, the source–reservoir pressure difference, and the matching degree of the physical properties of the upper and lower sandstones. Its overall accumulation efficiency is usually lower than that of the source–reservoir type and the favorable source–reservoir interbedded type.

5.2. Petrophysical Threshold of Sandstone Reservoirs According to Source–Reservoir Configuration

Uniform porosity and permeability cutoffs do not fully account for all oil-test outcomes. High porosity and permeability alone do not necessarily correspond to commercial oil production. Source rock hydrocarbon supply capacity and source–reservoir configuration should therefore be considered when interpreting petrophysical cutoffs under different geological conditions.

The oil content and productivity of interlayered shale oil sandstone reservoirs not only depend on the porosity and permeability of the sandstone itself but are also jointly controlled by the hydrocarbon supply capacity of the source rock, source–reservoir pressure difference, source–reservoir combination mode, and source–reservoir distance. In order to quantitatively characterize the synergy between the above factors, this study constructed a hydrocarbon supply potential index:

$$H_s = TOC * S_1 * R_o \quad (5)$$

where TOC is the total organic carbon content, %; S_1 is the pyrolysis free hydrocarbon content of the rock, mg/g; and R_o is the vitrinite reflectance, %. Among them, TOC reflects the abundance of organic matter in the source rock, S_1 represents the current movable or free hydrocarbon content, and Ro represents the degree of thermal evolution of organic matter.

On this basis, the source–reservoir coupling index is constructed based on the source–reservoir pressure difference, source–reservoir combination relationship and source–reservoir spatial configuration:

$$C_{sr} = \left(\frac{H_s}{H_{s0}}\right)^{0.6} \left(\frac{\Delta P}{\Delta P_0}\right)^{0.4} F_c F_d \quad (6)$$

C_{sr}: source–reservoir coupling index;

H_s: hydrocarbon generation potential, calculated using Equation (5);
ΔP: source–reservoir pressure difference;
H_{s0}, ΔP_0: normalization reference scale;
F_c: source–reservoir configuration coefficient;
F_d: source–reservoir distance coefficient.

In the formula, C_{sr} is the dimensionless source–reservoir coupling index. H_{s0} and ΔP_0 are normalization reference scales rather than physical cutoff values. Hs0 was set to 8.0, with the same composite unit as H_s, and ΔP was set to 5.0 MPa. Across the 20 tested intervals, Hs ranged from 0.756 to 17.227 (mean 6.854; median 4.529), and 8.0 corresponded approximately to the 55th empirical percentile. Delta P ranged from 1.001 to 10.177 MPa (mean 5.554 MPa; median 4.624 MPa), so 5.0 MPa represents a rounded central pressure scale. The ratios H_s/H_{s0} and $\Delta P/\Delta P_0$ therefore remove dimensional differences and place the two terms on comparable numerical scales. These reference values are specific to the present study area and are not universal geological thresholds.

If alternative positive reference scales $H_{s0}{}'$ and $\Delta P_0{}'$ are used, the recalculated index satisfies Equation (7).

$$C_{sr}{}' = \left(\frac{H_s{}'}{H_{s0}{}'}\right)^{0.6} \left(\frac{\Delta P'}{\Delta P_0{}'}\right)^{0.4} \quad (7)$$

Thus, changing either reference scale multiplies all intervals by the same constant and does not change their relative ranking, provided that the C_{sr} class boundaries are rescaled consistently. The normalization constants and the C_{sr} boundaries were therefore treated as a joint, study-area-specific parameterization.

The original values of F_c, F_d, H_{S0}, ΔP_0, and the coupling-class boundaries were held constant. Only the weights of H_S and the source–reservoir pressure difference were varied:

$$\omega = 0.4, 0.45, 0.5, \ldots, 0.8$$

The weight assigned to the pressure difference term was constrained as:

$$\omega_{\Delta P} = 1 - \omega$$

For each weighting scheme, C_{sr} was recalculated for all calibration intervals as follows:

$$C_{sr,i}(\omega) = \left(\frac{H_{s,i}}{8.0}\right)^{\omega} \left(\frac{\Delta P_i}{5.0}\right)^{1-\omega} F_{c,i} F_{d,i}$$

The predicted class of each interval was then determined using the fixed coupling boundaries:

$$y_i \begin{cases} Ineffective\ interval, & C_{sr,i} < 0.5 \\ Low - productivity\ oil\ interval, & 0.5 \le C_{sr,i} < 1.5 \\ Commercial\ oil\ interval, & C_{sr,i} \ge 0.5 \end{cases}$$

The results of the sensitivity analysis are presented in Table 2.

Table 2. Results of the sensitivity analysis.

H_s Weight	ΔP Weight	Accuracy	Balanced Accuracy	Macro-F1
0.40–0.55	0.60–0.45	75.0%	74.8%	73.9%
0.60–0.70	0.40–0.30	80.0%	80.4%	79.2%
0.75–0.80	0.25–0.20	75.0%	76.7%	75.0%

These results show that the reference 0.6/0.4 weighting scheme lies within a stable performance interval. However, it should not be interpreted as a uniquely optimal weighting scheme.

The weights of the hydrocarbon supply and pressure difference terms were fixed at 0.6 and 0.4, respectively. Candidate values were then assigned to F_c and F_d around their reference values. The source–reservoir distance is defined as the minimum vertical distance between the tested sandstone interval and the nearest effective source rock interval.

The candidate configuration coefficients were:

$$F_{c,source-in-reservoir} \in \{1.00,1.05,1.10,1.15,1.20\}$$

$$F_{c,reservoir-in-source} \in \{0.70,0.80,0.90\}$$

The coefficient for the source–reservoir interbedded configuration was fixed at:

$$F_{c,interbedded} = 1.00$$

The candidate distance coefficients were:

$$F_d(d = 0) \in \{1.05,1.15,1.25\}$$

$$F_d(0 < d \leq 2m) \in \{1.00,1.10,1.20\}$$

$$F_d(2 < d \leq 5m) \in \{0.90,1.00,1.10\}$$

$$F_d(5 < d \leq 10m) \in \{0.65,0.75,0.85\}$$

$$F_d(d > 10m) = 0.35$$

For each combination, C_{sr} was recalculated, and the intervals were classified using the fixed boundaries of 0.5 and 1.5. The following is one of the best-performing parameter combinations:

$$F_{c,source-in-reservoir} = 1.15$$

$$F_{c,reservoir-in-source} = 0.80$$

$$F_d = \{1.25,1.10,1.00,0.75,0.35\}$$

F_c is a relative configuration coefficient centered on the interbedded reference configuration (F_c = 1.00). Values of 1.15 and 0.80 were assigned to the source-sandwiched-reservoir and reservoir-sandwiched-source configurations, respectively, to represent their expected relative hydrocarbon supply efficiency. Fd is a monotonic distance coefficient: F_d = 1.25 at d = 0; 1.10 at 0 < d ≤ 2 m; 1.00 at 2 < d ≤ 5 m; 0.75 at 5 < d ≤ 10 m; and 0.35 at d > 10 m. These coefficients are relative adjustment factors encoding the expected ordering of contact and migration efficiency, rather than independently measured physical constants.

Using the reference parameterization, the source–reservoir relationship was classified as weak coupling when C_{sr} < 0.5, moderate coupling when 0.5 ≤ C_{sr} < 1.5, and strong coupling when C_{sr} ≥ 1.5. Comparison with the formation-test outcomes (Figure 13) shows that industrial oil intervals occur mainly in the strong coupling class, low-production intervals occur mainly in the moderate coupling class, and dry or water-bearing intervals occur mainly in the weak coupling class.

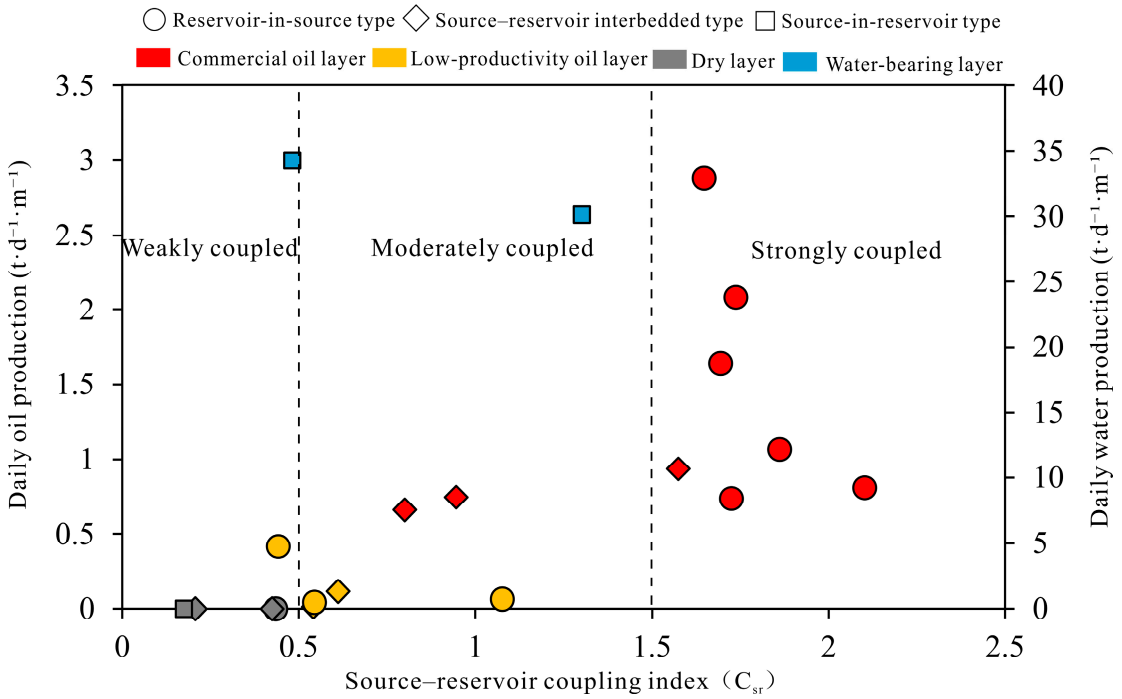


Figure 13. Source–reservoir coupling classification and its relationship with oil and water production.

The weight-sensitivity analysis showed that the reference weighting scheme lies within the best-performing interval. When the H_s exponent was 0.40–0.55, the overall accuracy, balanced accuracy, and macro-averaged F1 score were 75.0%, 74.8%, and 73.9%, respectively. All three metrics increased and remained constant at 80.0%, 80.4%, and 79.2% when the Hs exponent was 0.60–0.70, whereas the overall accuracy decreased to 75.0% at 0.75–0.80. Under the reference 0.6/0.4 parameterization, five of six ineffective intervals, four of five low-production intervals, and seven of nine industrial oil intervals were correctly classified. The constrained F_c–F_d grid analysis increased the maximum apparent accuracy from 80.0% to 85.0%, but 54 parameter combinations produced the same maximum result. Selecting one of these tied combinations post hoc would create a substantial overfitting risk. We therefore retained the original, geologically ordered F_c and F_d values as the reference parameterization.

The intersection relationship between the source–reservoir coupling index, porosity, and permeability shows that there are obvious differences in the lower limits of the physical properties of effective reservoirs under different coupling conditions (Figure 14). The estimated porosity and permeability cutoffs for strongly coupled intervals are approximately 6.5% and 0.12 mD, respectively. For moderately coupled intervals, the corresponding cutoffs increase to approximately 8.5% and 0.23 mD. The reservoir in the weak coupling zone is basically ineffective, mainly showing as a dry layer or a water layer. This result shows that the higher the degree of source–reservoir coupling, the lower the lower limit of reservoir physical properties required to form an effective oil layer. Under strong coupling conditions, sufficient hydrocarbon supply material base, strong migration force and short migration distance can compensate to a certain extent for the lack of sandstone storage space and seepage capacity, so some low-porosity and low-permeability sandstones can still form industrial oil layers. In contrast, under moderate or weak coupling conditions, sandstones require relatively high porosity and permeability to achieve effective charging and economic production.

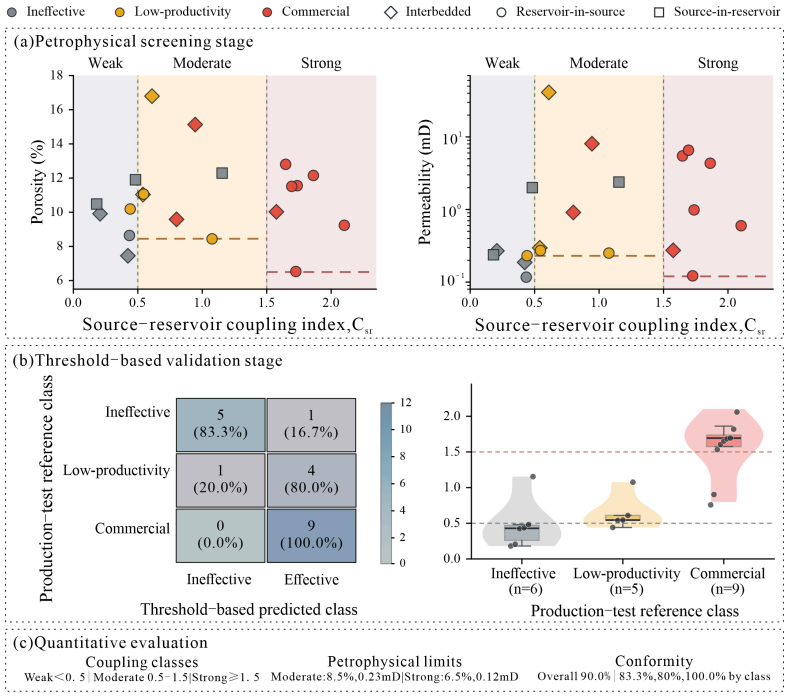


Figure 14. Intersection plot of the source–reservoir coupling index and physical property parameters.

5.3. Independent Validation of Coupling-Specific Petrophysical Thresholds

To evaluate the applicability of the proposed coupling-specific petrophysical thresholds, an independent dataset comprising 20 oil-test intervals that were not used for model calibration or threshold determination was examined (Figure 15). The previously established coupling boundaries and petrophysical thresholds were applied without recalibration. Of the 20 intervals, 17 were consistent with the production-test results, yielding an overall conformity of 85.0%. The conformity rates were 100.0% (5/5) for ineffective intervals, 87.5% (7/8) for low-productivity oil intervals, and 71.4% (5/7) for commercial oil intervals, with a mean class conformity of 86.3%. The three discordant intervals were all located in the weak coupling domain C_{sr} < 0.5 despite producing oil during testing, suggesting that most residual disagreement was associated with the weak coupling boundary. Overall, the independent results support the applicability of the coupling-specific thresholds to effective reservoir identification in the study area. However, given the limited size of the independent validation dataset, further evaluation using additional wells and oil-test intervals is still required to assess the broader applicability of the proposed thresholds.

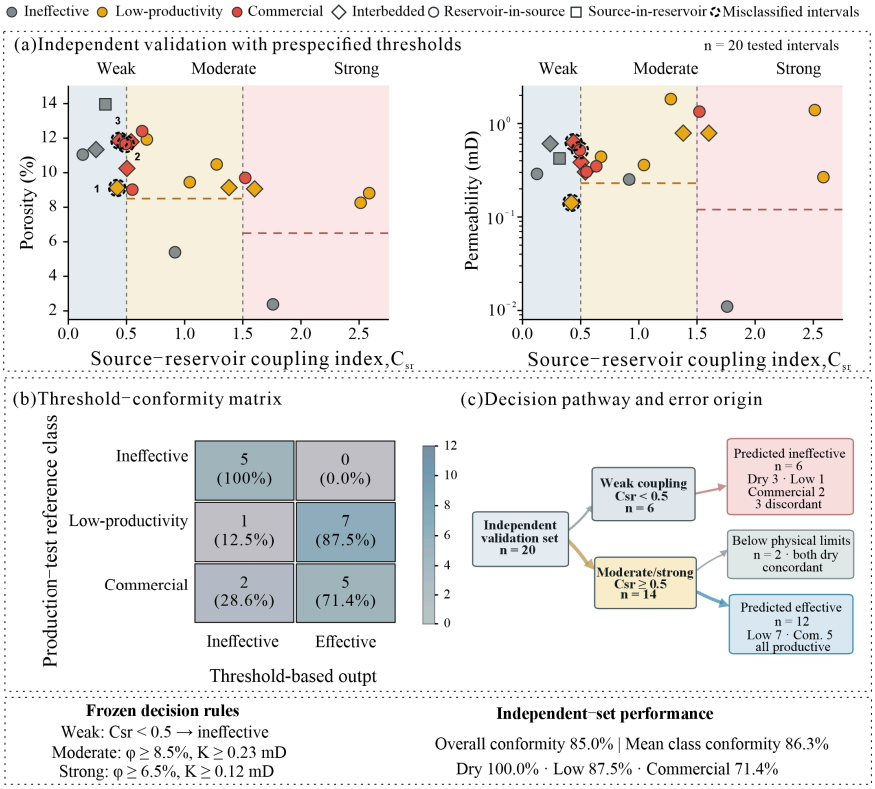


Figure 15. Independent validation of coupling-specific petrophysical thresholds using 20 oil-test intervals.

5.4. Comparison

To facilitate a direct comparison of the effective reservoir cutoffs derived using different methods and their geological applicability, Table 3 summarizes the evaluation criteria and cutoff values obtained from four conventional methods and the source–reservoir coupling approach.

Table 3. Comparison of the petrophysical cutoffs determined using different methods.

Method	Porosity Cutoff	Permeability Cutoff
Porosity–permeability cross-plot method	8.0%	0.09 mD
Mercury injection displacement pressure method	8.0%	0.11 mD
Minimum pore-throat radius method	8.8%	0.16 mD
Oil occurrence method	8.0%	0.08 mD
Source–reservoir coupling index	Strongly coupled: 6.5%	0.12 mD
	Moderately coupled: 8.5%	0.23 mD

The porosity cutoffs derived from the four conventional methods range from 8.0% to 8.8%, whereas the permeability cutoffs range from 0.08 to 0.13 mD. Their general consistency indicates that these methods primarily characterize the storage capacity, pore-throat structure, and fluid-flow capability of the sandstone reservoir itself. However, because they apply relatively uniform petrophysical cutoffs, these methods cannot adequately explain why some high-porosity and high-permeability intervals remain dry or water-bearing under weak source–reservoir coupling, whereas intervals with porosities below the conventional cutoff may still yield commercial oil production under strong coupling.

The source–reservoir coupling approach further reveals that the effective reservoir cutoffs vary systematically with coupling intensity. Under moderate coupling, the porosity and permeability cutoffs are approximately 8.5% and 0.23 mD, respectively, whereas under strong coupling, they decrease to approximately 6.5% and 0.12 mD. Thus, the source–reservoir coupling approach shifts reservoir evaluation from an assessment based solely on sandstone storage and flow capacity to an integrated evaluation of the entire hydrocarbon supply–charging–storage–flow process. The resulting reservoir cutoffs are not fixed empirical values but dynamic geological thresholds that vary with the degree of source–reservoir coupling.

Figure 16 compares the classification performance of four conventional petrophysical cutoff methods and the source–reservoir coupling approach using 20 independent oil-test intervals. The coupling approach did not improve overall accuracy. However, it reduced the misclassification of ineffective intervals as effective and achieved more balanced classification performance.

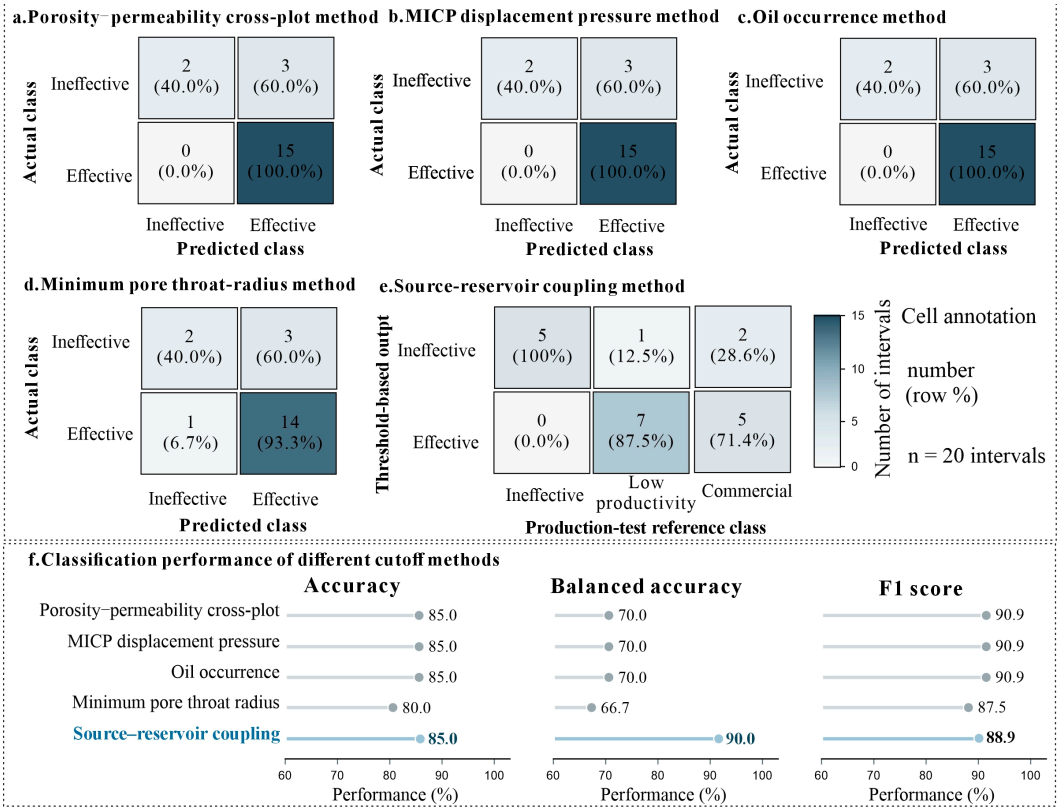


Figure 16. Comparison of reservoir cutoff methods.

Therefore, compared with uniform porosity–permeability cutoffs, this approach provides a more geologically constrained basis for effective reservoir identification within the study area and helps explain variations in hydrocarbon accumulation, thereby supporting sweet spot interval selection and resource assessment in interbedded shale oil systems.

6. Conclusions

The intercalated shale oil source rocks in the study area are generally at a medium to good source rock level, and some have reached high-quality source rock. The organic matter abundance is high, mainly type I and type II_1 oil-generating organic matter, and the degree of thermal evolution is mainly in the mature stage. The sandstone reservoir is mainly feldspar lithic sandstone, and the reservoir space is dominated by intergranular

pores and secondary dissolved pores. Oil and gas are mainly distributed in intergranular pores, and heavy components are higher than light components.

There are three main types of source–reservoir configuration: source–storage type, source–reservoir interlayer type, and reservoir–source type. The source–reservoir type has the characteristics of bidirectional hydrocarbon supply, large source–reservoir contact area, and short migration distance. It usually has higher accumulation efficiency and is one of the most favorable source–reservoir configurations for interlayered shale oil. The source–reservoir interbedded type is conducive to improving the overall hydrocarbon supply efficiency, but the oil content of different sandstone interlayers is still controlled by the thickness of the single layer, lateral continuity, pore-throat structure and the quality of adjacent source rocks. The effectiveness of the reservoir intercalation source type is more dependent on the hydrocarbon supply intensity of the source rock, the source–reservoir pressure difference and the matching degree of the physical properties of the upper and lower sandstones.

Based on parameters such as total organic carbon content, free hydrocarbon content, vitrinite reflectivity, source–reservoir pressure difference, source–reservoir combination relationship, and source–reservoir distance, a source–reservoir coupling index C_{sr} was established. According to the source–reservoir coupling index, the source–reservoir relationship in the study area can be divided into three categories: weak coupling, medium coupling, and strong coupling. Industrial oil layers are mainly distributed in strong coupling areas, and some are located in medium coupling areas; low-yield oil layers are mainly distributed in medium coupling areas, and a small amount enters weak coupling areas; dry layers and water layers are generally weakly coupled. Compared with evaluations based on uniform porosity and permeability cutoffs, this approach additionally considers source rock hydrocarbon supply capacity and source–reservoir configuration. It provides a complementary basis for explaining low-petrophysical-quality oil-producing intervals and high-petrophysical-quality ineffective intervals while offering geological constraints for effective reservoir identification, sweet spot evaluation, and favorable zone selection within the study area.

Author Contributions: S.Y.: Writing—original draft, methodology, data curation, and conceptualization. J.Z.: Writing—review and editing, supervision, and funding acquisition. L.F.: Methodology and writing—review and editing. J.H.: Methodology and data curation. Z.W.: Writing—review and editing. Z.Z.: Methodology and data curation. W.W.: Methodology and investigation. G.W.: Validation and supervision. P.X.: Data curation. All authors have read and agreed to the published version of the manuscript.

Funding: This work was financially supported by the National Science and Technology Major Project of China (2025ZD1403902), the National Science and Technology Major Project of China (2024ZD1404902), the Science Foundation of China University of Petroleum, Beijing (No. 2462025BJRC010), and the major science and technology project administered by the China National Petroleum Corporation (Grant No. 2023ZZ15YJ02).

Data Availability Statement: The raw data supporting the conclusions of this article will be made available by the authors on request.

Acknowledgments: This work was financially supported by the National Science and Technology Major Project of China (2024ZD1404902), the Science Foundation of China University of Petroleum, Beijing (No. 2462025BJRC010), and the major science and technology project administered by the China National Petroleum Corporation (Grant No. 2023ZZ15YJ02). We are also grateful to the editor and reviewers for providing excellent advice on the manuscript.

Conflicts of Interest: Authors Shujun Yin, Jiandong Zheng, Zhaoqian Zhang, Wenjuan Wang and Peng Xie were employed by the company Exploration and Development Research Institute, PetroChina Daqing Oilfield Co., Ltd.. Author Limin Fang was employed by the company Exploration Department of PetroChina Daqing Oilfield Co., Ltd.. Author Jin Hu was employed by the company PetroChina Daqing Oilfield Co., Ltd.. The remaining authors declare that the research was conducted in the absence of any commercial or financial relationships that could be construed as a potential conflict of interest.

References

1. Soeder, D.J. The successful development of gas and oil resources from shales in North America. *J. Pet. Sci. Eng.* **2018**, *163*, 399–420. https://doi.org/10.1016/j.petrol.2017.12.084.
2. Jin, Z.; Liang, X.; Bai, Z. Exploration breakthrough and its significance of Gulong lacustrine shale oil in the Songliao Basin, northeastern China. *Energy Geosci.* **2022**, *3*, 120–125. https://doi.org/10.1016/j.engeos.2022.01.005.
3. Pang, X.; Wang, G.; Mountney, N.P.; Kuang, L.; Zhao, X.; Zhao, Y.; Li, H.; Han, Z.; Tian, H. Prediction of lamina structure and reservoir quality in shale using well logs: The Cretaceous Qingshankou Formation, Gulong Sag, Songliao Basin, China. *Geoenergy Sci. Eng.* **2023**, *227*, 211827. https://doi.org/10.1016/j.geoen.2023.211827.
4. Wang, H.; Ma, F.; Tong, X.; Liu, Z.; Zhang, X.; Wu, Z.; Li, D.; Wang, B.; Xie, Y.; Yang, L. Assessment of global unconventional oil and gas resources. *Pet. Explor. Dev.* **2016**, *43*, 925–940. https://doi.org/10.1016/S1876-3804(16)30111-2.
5. Solarin, S.A. The effects of shale oil production, capital, and labour on economic growth in the United States: A maximum-likelihood analysis of the resource curse hypothesis. *Resour. Policy* **2020**, *68*, 101799. https://doi.org/10.1016/j.resourpol.2020.101799.
6. Shakya, S.; Li, B.; Etienne, X. Shale revolution, oil and gas prices, and drilling activities in the United States. *Energy Econ.* **2022**, *108*, 105877. https://doi.org/10.1016/j.eneco.2022.105877.
7. Rodhan, M.A. The effect of US shale oil production on local and international oil markets. *Int. J. Energy Econ. Policy* **2023**, *13*, 433–443. https://doi.org/10.32479/ijeep.14455.
8. Zhao, X.; Liu, Y.; Wu, Z.; Dong, H.; Liu, X.; Yang, R.; Zhang, H.; Liu, Z.; Li, J.; Ma, C. Diversity of continental shale oil in China. *Earth-Sci. Rev.* **2026**, *281*, 105589. https://doi.org/10.1016/j.earscirev.2026.105589.
9. Baskoro, A.S.; Baur, F.; Yu, A.Z.; Grossman, E.L. Restoring source-rock initial quality and quantity with kinetic-based inversion—Applied to the Wolfcamp play in the Permian Delaware Basin. *Mar. Pet. Geol.* **2023**, *150*, 106143. https://doi.org/10.1016/j.marpetgeo.2023.106143.
10. Wang, X.; Grossman, E.L.; Becker, M.R. High-resolution chemofacies and pore-system characterization of the Pennsylvanian Cline Shale, Midland Basin, Texas. *Mar. Pet. Geol.* **2024**, *170*, 107120. https://doi.org/10.1016/j.marpetgeo.2024.107120.
11. Liu, X.; Nordeng, S.H.; Chen, Z.; Jiang, C.; Mort, A. Organic matter variation within the Upper and Lower Bakken shales of the Williston Basin by extracting kerogen pyrogram information. *Int. J. Coal Geol.* **2020**, *229*, 103574. https://doi.org/10.1016/j.coal.2020.103574.
12. Henderson, K.M.; Williams-Jones, A.E.; Sahoo, S.; Jiang, C.; Nesheim, T.O. A diagenetic shale source for lithium in oilfield brines: Insights from the Devonian Bakken–Three Forks system, Williston Basin. *Chem. Geol.* **2026**, *706*, 123270. https://doi.org/10.1016/j.chemgeo.2026.123270.
13. Tunstall, T. Iterative Bass model forecasts for unconventional oil production in the Eagle Ford Shale. *Energy* **2015**, *93*, 580–588. https://doi.org/10.1016/j.energy.2015.09.072.
14. Hou, L.; Zhao, Z.; Wu, S.; Hou, M.; Wang, Z.; Lin, S.; Yang, Z.; Li, S.; Zhang, M.; Luo, X. Dynamic evolution mechanism of petrophysical properties in shale reservoirs and its petroleum geological significance: A case study of the Cretaceous Lower Eagle Ford Formation, Gulf Coast Basin, USA. *Pet. Explor. Dev.* **2026**, *53*, 311–326. https://doi.org/10.1016/S1876-3804(26)60694-5.
15. Mazzini, A.; Svensen, H.; Leanza, H.A.; Corfu, F.; Planke, S. Early Jurassic shale chemostratigraphy and U–Pb ages from the Neuquén Basin, Argentina: Implications for the Toarcian Oceanic Anoxic Event. *Earth Planet. Sci. Lett.* **2010**, *297*, 633–645. https://doi.org/10.1016/j.epsl.2010.07.017.
16. Raef, A.E.; Kamari, A.; Totten, M.; Harris, D.; Janssen, K.; Lambert, M. Dynamic elastic and mineralogical brittleness of the Woodford Shale of the Anadarko Basin: Ultrasonic P-wave and S-wave velocities, XRD mineralogy, and predictive models. *J. Pet. Sci. Eng.* **2018**, *169*, 33–43. https://doi.org/10.1016/j.petrol.2018.05.052.

17. Uzun, O.; Kazemi, H. Assessment of enhanced oil recovery by osmotic pressure in unconventional reservoirs: Application to Niobrara Chalk and Codell Sandstone. *Fuel* **2021**, *306*, 121270. https://doi.org/10.1016/j.fuel.2021.121270.
18. Balumi, W.B.; ElGhonimy, R.S.; Sonnenberg, S.; Puckette, J. Chemostratigraphy of unconventional shale reservoirs: A case study of the Niobrara Formation within the Denver–Julesburg Basin. *Mar. Pet. Geol.* **2022**, *146*, 105957. https://doi.org/10.1016/j.marpetgeo.2022.105957.
19. Burnaz, L.; Kalmykov, A.; Grohmann, S.; Kalmykov, G.; Littke, R. Geochemistry and organic petrology of organic-rich shales of the Upper Jurassic–Lower Cretaceous Bazhenov Horizon in the Frolov region, West Siberian Basin: Implications for the reconstruction of organic matter origin and paleoredox conditions. *Mar. Pet. Geol.* **2022**, *143*, 105809. https://doi.org/10.1016/j.marpetgeo.2022.105809.
20. Konstantinovskaya, E.; He, Q.; Hall, D.; Phiukhao, W.; Steele-MacInnis, M.; Harris, N.B.; Rodriguez, G.G. Fracture systems and fluid inclusions in Upper Devonian organic-rich shales in the Western Canada Sedimentary Basin and Rocky Mountains foreland belt, west-central Alberta, Canada. *Earth-Sci. Rev.* **2025**, *271*, 105282. https://doi.org/10.1016/j.earscirev.2025.105282.
21. Yang, Y.; Cao, X.; Zhang, S.; Lyu, Q.; Liu, Z.; Sun, H.; Li, W.; Lu, G.; Chen, L. Key scientific issues and research progress in the development of shale oil in the Jiyang Depression, Bohai Bay Basin, China. *Pet. Explor. Dev.* **2026**, *53*, 167–180. https://doi.org/10.1016/S1876-3804(26)60682-9.
22. Yuan, S.; Lin, M.; Xi, K.; Wang, X.; Feng, S.-B.; Liu, J.; Li, K.; Cao, Y. Stratigraphic records of volcanic activity and their influence on the development of organic-rich shale in the Chang 7_3 submember of the Yanchang Formation, Ordos Basin. *J. Palaeogeogr.* **2026**, *15*, 100361. https://doi.org/10.1016/j.jop.2026.100361.
23. Zhao, W.; Liu, S.; Bian, C.; Song, Y.; Gao, G.; Liu, W.; Li, Y.; Fan, K.; Dong, J.; Guan, M. 'Component flow' of shale oil and its significance for sweet-spot evaluation in the Permian Lucaogou Formation, Jimsar Sag, Junggar Basin, China. *Pet. Explor. Dev.* **2026**, *53*, 612–624. https://doi.org/10.1016/S1876-3804(26)60715-X.
24. Zhu, R.; Zhang, Z.; Feng, C.; Shao, M.; Miao, X.; Zhang, D.; Liang, Y. Research progress, challenges, and prospects of continental shale oil. *Pet. Explor. Dev.* **2026**, *53*, 708–722. https://doi.org/10.1016/S1876-3804(26)60721-5.
25. Liu, B.; Shi, J.; Fu, X.; Lyu, Y.; Sun, X.; Gong, L.; Bai, Y. Petrological characteristics and shale oil enrichment of a lacustrine fine-grained sedimentary system: A case study of organic-rich shale in the first member of the Cretaceous Qingshankou Formation in the Gulong Sag, Songliao Basin, NE China. *Pet. Explor. Dev.* **2018**, *45*, 884–894. https://doi.org/10.1016/S1876-3804(18)30091-0.
26. Liu, B.; Sun, J.; Zhang, Y.; He, J.; Fu, X.; Yang, L.; Xing, J.; Zhao, X. Reservoir space and enrichment model of shale oil in the first member of the Cretaceous Qingshankou Formation in the Changling Sag, southern Songliao Basin, NE China. *Pet. Explor. Dev.* **2021**, *48*, 608–624. https://doi.org/10.1016/S1876-3804(21)60049-6.
27. Sun, L.; Liu, H.; He, W.; Li, G.; Zhang, S.; Zhu, R.; Jin, X.; Meng, S.; Jiang, H. An analysis of major scientific problems and research paths of Gulong shale oil in Daqing Oilfield, NE China. *Pet. Explor. Dev.* **2021**, *48*, 527–540. https://doi.org/10.1016/S1876-3804(21)60043-5.
28. Sun, L.; Zhu, R.; Zhang, T.; Cai, Y.; Feng, Z.; Bai, B.; Jiang, H.; Wang, B. Advances and trends in non-marine shale sedimentology: A case study of the Gulong shale in the Daqing Oilfield, Songliao Basin, NE China. *Pet. Explor. Dev.* **2024**, *51*, 1367–1385. https://doi.org/10.1016/S1876-3804(25)60547-7.
29. Wardlaw, N.C.; Taylor, R.P. Mercury capillary-pressure curves and the interpretation of pore structure and capillary behavior in reservoir rocks. *Bull. Can. Pet. Geol.* **1976**, *24*, 225–262.
30. Worthington, P.F.; Cosentino, L. The role of cutoffs in integrated reservoir studies. *SPE Reserv. Eval. Eng.* **2005**, *8*, 276–290. https://doi.org/10.2118/84387-PA.
31. Bai, B.; Zhu, R.; Wu, S.; Cui, J.; Su, L.; Li, T. New pore-throat structure characterization techniques for unconventional tight hydrocarbon reservoirs and their significance. *China Pet. Explor.* **2014**, *19*, 78–86.
32. Wang, Y.; Cao, Y.; Song, G.; Song, L.; Yang, T.; Zhang, S. Analysis of petrophysical cutoffs of reservoir intervals with production capacity and accumulation capacity in clastic reservoirs. *Pet. Sci.* **2014**, *11*, 211–219. https://doi.org/10.1007/s12182-014-0334-5.
33. Pittman, E.D. Relationship of porosity and permeability to various parameters derived from mercury injection–capillary pressure curves for sandstone. *AAPG Bull.* **1992**, *76*, 191–198. https://doi.org/10.1306/BDFF87A4-1718-11D7-8645000102C1865D.
34. Lai, J.; Wang, G.; Wang, Z.; Chen, J.; Pang, X.; Wang, S.; Zhou, Z.; He, Z.; Qin, Z.; Fan, X. A review on pore structure characterization in tight sandstones. *Earth-Sci. Rev.* **2018**, *177*, 436–457. https://doi.org/10.1016/j.earscirev.2017.12.003.
35. Shi, B.; Chang, X.; Liu, Z.; Liu, Y.; Ge, T.; Zhang, P.; Wang, Y.; Wang, Y.; Mao, L. Physical-property cutoffs of tight reservoirs determined from field and laboratory experiments: A case study of the Chang 6 and Chang 8–9 members, Ordos Basin. *Front. Earth Sci.* **2021**, *15*, 471–489. https://doi.org/10.1007/s11707-020-0851-z.

36. Han, C.; Qi, M.; Ma, C.; Zhao, L.; Lei, L.; Kong, W.; Li, Z.; Li, J.; Lv, N.; Cao, X. Determination of the lower limit of physical properties of tight oil reservoirs: A case study of the lower Es3 in the Jiangjiadian area, Linnan Sag. *ACS Omega* **2023**, *8*, 35856–35865. https://doi.org/10.1021/acsomega.3c03379.
37. Guo, X.; Wang, E.; Ma, X.; Li, M.; Qian, M.; Cao, T.; Li, Z.; Chu, J. Lacustrine shale oil systems in China: Advances in characterization methods and resource accumulation models. *Earth-Sci. Rev.* **2025**, *270*, 105256. https://doi.org/10.1016/j.earscirev.2025.105256.
38. Aguilera, R. Flow units: From conventional to tight-gas to shale-gas to tight-oil to shale-oil reservoirs. *SPE Reserv. Eval. Eng.* **2014**, *17*, 190–208. https://doi.org/10.2118/165360-PA.
39. Zhou, N.; Lu, S.; Wang, M.; Huang, W.; Xiao, D.; Jiao, C.; Wang, J.; Tian, W.; Zhou, L.; Chen, F.; et al. Limits and grading evaluation criteria of tight oil reservoirs in typical continental basins of China. *Pet. Explor. Dev.* **2021**, *48*, 1089–1100. https://doi.org/10.1016/S1876-3804(21)60093-9.
40. Hu, T.; Pang, X.; Jiang, F.; Wang, Q.; Liu, X.; Wang, Z.; Jiang, S.; Wu, G.; Li, C.; Xu, T.; et al. Movable oil content evaluation of lacustrine organic-rich shales: Methods and a novel quantitative evaluation model. *Earth-Sci. Rev.* **2021**, *214*, 103545. https://doi.org/10.1016/j.earscirev.2021.103545.
41. Huo, Z.; Hao, S.; Liu, B.; Zhang, J.; Ding, J.; Tang, X.; Li, C.; Yu, X. Geochemical characteristics and hydrocarbon expulsion of source rocks in the first member of the Qingshankou Formation in the Qijia–Gulong Sag, Songliao Basin, northeast China: Evaluation of shale oil resource potential. *Energy Sci. Eng.* **2020**, *8*, 1450–1467. https://doi.org/10.1002/ese3.603.
42. Song, Y.; Luo, Q.; Jiang, Z.; Yang, W.; Liu, D. Enrichment of tight oil and its controlling factors in central and western China. *Pet. Explor. Dev.* **2021**, *48*, 492–506. https://doi.org/10.1016/S1876-3804(21)60040-X.
43. Wang, F.; Chen, D.; Yao, D.; Cheng, M.; Wang, Q.; Tian, Z.; Du, W.; Wang, C.; Chang, S.; Jiang, M. Disparities in tight sandstone reservoirs in different source–reservoir assemblages and their effect on tight oil accumulation: Triassic Chang 7 Member in the Qingcheng area, Ordos Basin. *J. Pet. Sci. Eng.* **2022**, *217*, 110914. https://doi.org/10.1016/j.petrol.2022.110914.
44. Wang, P.-J.; Mattern, F.; Didenko, N.A.; Zhu, D.-F.; Singer, B.; Sun, X.-M. Tectonics and cycle system of the Cretaceous Songliao Basin: An inverted active continental margin basin. *Earth-Sci. Rev.* **2016**, *159*, 82–102. https://doi.org/10.1016/j.earscirev.2016.05.004.
45. Meng, Q.; Zhou, Z.; Zhu, R.; Xu, Y.; Guo, Z. Cretaceous basin evolution in northeast Asia: Tectonic responses to Paleo-Pacific Plate subduction. *Natl. Sci. Rev.* **2022**, *9*, nwab088. https://doi.org/10.1093/nsr/nwab088.
46. Sun, L.; Jin, W.; Fu, B.; Wang, J.; Feng, Z.; Zhang, J. Nano-scale occurrence classification of laminated Gulong shale oil and gas. *Pet. Geol. Oilfield Dev. Daqing* **2025**, *44*, 1–11. https://doi.org/10.19597/J.ISSN.1000-3754.202509034.
47. Huang, Y.; Jiang, Q.; Chang, J.; Qiu, N.; Zhou, Y.; Kang, H.; Zhang, M. Fluid inclusion analysis and carbonate U–Pb dating reveal shale oil accumulation processes in the Qingshankou Formation, Songliao Basin, NE China. *Pet. Sci.* **2026**, *23*, 6053–6069. https://doi.org/10.1016/j.petsci.2026.06.054.
48. Liu, B.; Zhang, J.; Bai, L.; Fu, X.; Liu, Y.; Wang, B.; Wu, J. Temperature–pressure history of the Cretaceous Qingshankou Formation and its relationship with Gulong shale oil enrichment in the northern Songliao Basin, China. *Pet. Explor. Dev.* **2026**, *53*, 757–769. https://doi.org/10.1016/S1876-3804(26)60724-0.
49. Feng, Z.; Jia, C.; Xie, X.; Zhang, S.; Feng, Z.; Cross, T.A. Tectonostratigraphic units and stratigraphic sequences of the nonmarine Songliao Basin, northeast China. *Basin Res.* **2010**, *22*, 79–95. https://doi.org/10.1111/j.1365-2117.2009.00445.x.
50. Zhao, Z.; Littke, R.; Zieger, L.; Hou, D.; Froidl, F. Depositional environment, thermal maturity, and shale oil potential of the Cretaceous Qingshankou Formation in the eastern Changling Sag, Songliao Basin, China: An integrated organic and inorganic geochemistry approach. *Int. J. Coal Geol.* **2020**, *232*, 103621. https://doi.org/10.1016/j.coal.2020.103621.
51. Yang, X.; Wang, H.; Li, Z.; Guan, C.; Wang, X. Tectonic–sedimentary evolution of a continental rift basin: A case study of the Early Cretaceous Changling and Lishu fault depressions, southern Songliao Basin, China. *Mar. Pet. Geol.* **2021**, *128*, 105068. https://doi.org/10.1016/j.marpetgeo.2021.105068.
52. Lyu, D.; Wang, H.; Li, G.; Zhang, J.; Fu, X.; Liu, C.; Wang, X.; Zhu, R.; Zhang, S. Paleobiological evidence of paleo-water-environment evolution during deposition of the Qingshankou shale in the Songliao Basin. *Oil Gas. Geol.* **2023**, *44*, 857–868. https://doi.org/10.11743/ogg20230405.
53. Liu, Y.; Wang, H.; Zhang, J.; Liu, Z.; Chen, F.; Wang, X.; Zhang, S.; Liu, H. Rare-earth-element and Sr-isotopic evidence for a seawater intrusion event in the Songliao Basin 91 million years ago. *Pet. Sci.* **2023**, *20*, 1347–1362. https://doi.org/10.1016/j.petsci.2022.11.015.

54. Chen, R.; Bai, X.; Huang, C.; Wu, X.; Shang, F. How marine incursions affect the sedimentary environment and the quality of source rocks in the Upper Cretaceous Songliao Basin, NE China. *Mar. Pet. Geol.* **2024**, *170*, 107140. https://doi.org/10.1016/j.marpetgeo.2024.107140.
55. Wu, H.; Zhang, S.; Jiang, G.; Huang, Q. The floating astronomical time scale for the terrestrial Late Cretaceous Qingshankou Formation from the Songliao Basin of northeast China and its stratigraphic and paleoclimate implications. *Earth Planet. Sci. Lett.* **2009**, *278*, 308–323. https://doi.org/10.1016/j.epsl.2008.12.016.
56. Bai, X.; Chen, R.; Shang, F.; Zhang, N. Sedimentary environment and oil-bearing characteristics of shale in the Cretaceous Qingshankou Formation, Songliao Basin. *Pet. Geol. Exp.* **2025**, *46*, 1063–1074. https://doi.org/10.11781/sysydz2024051063.
57. Zhou, B.; Xiao, Y.; Lei, Z.; Wang, R.; Hu, S.; Hou, X. Controlling factors for oil production in continental shales: A case study of the Cretaceous Qingshankou Formation in the Songliao Basin. *Pet. Res.* **2023**, *8*, 183–191. https://doi.org/10.1016/j.ptlrs.2023.05.003.
58. Yao, Q.; Xu, C.; Li, T.; Shao, S.; Li, C.; Wang, M.; Zheng, Y.; Liu, X. Differential reservoir formation mechanisms of shale oil reservoirs in the Qingshankou Formation, Cretaceous System, Songliao Basin. *Sci. Rep.* **2026**, *16*, 16127. https://doi.org/10.1038/s41598-026-47411-y.
59. Zhu, G.; Wang, X.; Zhang, J.; Liu, Z.; Bai, Y.; Zhao, Y.; Fu, X.; Zeng, H. Enrichment conditions and favorable zones for exploration and development of continental shale oil in the Songliao Basin. *Acta Pet. Sin.* **2023**, *44*, 110–124. https://doi.org/10.7623/syxb202301007.
60. Sun, L.; Jia, C.; Zhang, J.; Cui, B.; Bai, J.; Huo, Q.; Xu, X.; Liu, W.; Zeng, H.; Liu, W. Resource potential of Gulong shale oil in key areas of the Songliao Basin. *Acta Pet. Sin.* **2024**, *45*, 1699–1714.
61. Zhang, J.; Kang, D.; Wang, J.; Wu, W.; Yu, D.; Song, Y.; Yu, T.; Meng, D. Lithofacies types, oil-bearing characteristics, and controls on oil enrichment in interbedded shale reservoirs of the Qingshankou Formation, northern Songliao Basin. *Pet. Geol. Oilfield Dev. Daqing* **2026**, *advance online publication*. https://doi.org/10.19597/J.ISSN.1000-3754.202602016.
62. *GB/T 19145-2022*; Determination for Total Organic Carbon in Sedimentary Rock. Standards Press of China: Beijing, China, 2022. (In Chinese)
63. *GB/T 18602-2012*; Rock Pyrolysis Analysis. Standards Press of China: Beijing, China, 2012. (In Chinese)
64. *SY/T 5125-1996*; Transmitted Light–Fluorescence Kerogen Maceral Identification and Type Classification Method. Petroleum Industry Press: Beijing, China, 1996. (In Chinese)
65. *SY/T 5124-2012*; Determination of Vitrinite Reflectance in Sedimentary Rocks. Petroleum Industry Press: Beijing, China, 2012. (In Chinese)
66. *SY/T 7773-2024*; Laser Confocal Analysis Method for Rock Pore Structure. Petroleum Industry Press: Beijing, China, 2024. (In Chinese)
67. *GB/T 29171-2023*; Rock Capillary Pressure Measurement. Standards Press of China: Beijing, China, 2023. (In Chinese)
68. *SY/T 5368-2016*; Identification for Thin Sections of Rocks. Petroleum Industry Press: Beijing, China, 2016. (In Chinese)
69. *SY/T 5162-2021*; Scanning Electron Microscopy Analysis Method for Rock Samples. Petroleum Industry Press: Beijing, China, 2021. (In Chinese)
70. *GB/T 29172-2012*; Practices for Core Analysis. Standards Press of China: Beijing, China, 2012. (In Chinese)
71. Abrams, M.A.; Gong, C.; Garnier, C.; Sephton, M.A. A new thermal extraction protocol to evaluate liquid-rich unconventional oil in place and in-situ fluid chemistry. *Mar. Pet. Geol.* **2017**, *88*, 659–675. https://doi.org/10.1016/j.marpetgeo.2017.09.014.
72. Wang, Y.; Liang, J.; Zhang, J.; Zhao, B.; Zhao, Y.; Liu, X.; Xia, D. Resource potential and exploration direction of Gulong shale oil in the Songliao Basin. *Pet. Geol. Oilfield Dev. Daqing* **2020**, *39*, 20–34. https://doi.org/10.19597/J.ISSN.1000-3754.202005032.
73. Wu, Y.; Liu, C.; Jiang, F.; Hu, T.; Lv, J.; Zhang, C.; Guo, X.; Huang, L.; Hu, M.; Huang, R.; et al. Geological characteristics and shale oil potential of alkaline lacustrine source rocks in the Fengcheng Formation of the Mahu Sag, Junggar Basin, western China. *J. Pet. Sci. Eng.* **2022**, *216*, 110823. https://doi.org/10.1016/j.petrol.2022.110823.
74. Li, C.; Liu, X.; Meng, L.; Wang, J.; Gao, Y.; Sun, B.; Hua, Z. Fractal heterogeneity characteristics and influencing factors of lacustrine shale pore structure based on N2 adsorption and mercury injection in the Paleogene Shahejie Formation, Bohai Bay Basin, China. *Pet. Res.* **2026**, *advance online publication*. https://doi.org/10.1016/j.ptlrs.2026.01.019.
75. Wang, L.; Liu, B.; Bai, L.-H.; Ostadhassan, M.; Gentzis, T.; Wang, B.; Wang, Y. Maceral evolution of lacustrine shale and its effects on organic-pore development from the low-maturity to high-maturity stages: A case study of the Qingshankou Formation in the northern Songliao Basin, northeast China. *Pet. Sci.* **2023**, *20*, 2709–2725. https://doi.org/10.1016/j.petsci.2023.08.025.
76. Peters, K.E.; Cassa, M.R. Applied source rock geochemistry. *Pet. Syst. Source Trap AAPG Mem.* **1994**, *60*, 93–120. https://doi.org/10.1306/M60585C5.

77. Zhang, S.; Zhang, B.; Wang, X.; Feng, Z.; He, K.; Wang, H.; Fu, X.; Liu, Y.; Yang, C. Gulong shale oil enrichment mechanism and orderly distribution of conventional–unconventional oils in the Cretaceous Qingshankou Formation, Songliao Basin, NE China. *Pet. Explor. Dev.* **2023**, *50*, 1045–1059. https://doi.org/10.1016/S1876-3804(23)60448-3.
78. Cheng, H.; Li, D.; Bai, X.; Jiang, L.; Huang, Q.; Wang, D.; Wang, H.; Xu, S.; Wu, X.; Duan, W.; et al. Sedimentological and reservoir characteristics of Carboniferous–Permian shales in the northern Songliao Basin and surrounding areas, northeastern China. *J. Asian Earth Sci.* **2026**, *310*, 107192. https://doi.org/10.1016/j.jseaes.2026.107192.
79. Peters, K.E. Guidelines for evaluating petroleum source rock using programmed pyrolysis. *AAPG Bull.* **1986**, *70*, 318–329. https://doi.org/10.1306/94885688-1704-11D7-8645000102C1865D.
80. Grassmann, S.; Cramer, B.; Delisle, G.; Messner, J.; Winsemann, J. Geological history and petroleum system of the Mittelplate oil field, northern Germany. *Int. J. Earth Sci.* **2005**, *94*, 979–989. https://doi.org/10.1007/s00531-005-0018-x.
81. Xu, Y.; Lun, Z.; Pan, Z.; Wang, H.; Zhou, X.; Zhao, C.; Zhang, D. Occurrence space and state of shale oil: A review. *J. Pet. Sci. Eng.* **2022**, *211*, 110183. https://doi.org/10.1016/j.petrol.2022.110183.
82. Fu, J.; Luo, A.; Zhang, N.; Deng, X.; Lv, J.; Wu, K.; Wang, K.; Liu, L. Determining the lower limits of petrophysical properties of effective reservoirs in the Chang 7 oil-bearing interval, Ordos Basin. *China Pet. Explor.* **2014**, *19*, 82–88. https://doi.org/10.3969/j.issn.1672-7703.2014.06.0010.
83. Wang, J.; Cao, Y.; Gao, Y.; Liu, H.; Liu, X.; Tang, D. Petrophysical parameter cutoffs and controlling factors of effective Paleogene red-bed sandstone reservoirs in the Dongying Depression. *J. China Univ. Pet.* **2011**, *35*, 27–33. https://doi.org/10.3969/j.issn.1673-5005.2011.04.005.
84. Xiao, H.; Hu, T.; Pang, X.; Xu, Y.; Hu, Y.; Li, C.; Xu, T.; Zheng, D.; Pu, T.; Ding, C.; et al. A new method for identifying effective hydrocarbon source rocks and evaluating their relative contributions to reservoirs. *Mar. Pet. Geol.* **2025**, *178*, 107424. https://doi.org/10.1016/j.marpetgeo.2025.107424.

Disclaimer/Publisher's Note: The statements, opinions and data contained in all publications are solely those of the individual author(s) and contributor(s) and not of MDPI and/or the editor(s). MDPI and/or the editor(s) disclaim responsibility for any injury to people or property resulting from any ideas, methods, instructions or products referred to in the content.